

Septin-microtubule association via a motif unique to the isoform 1 of septin 9 tunes stress fibers

Mira Kuzmić¹, Gerard Castro Linares², Jindřiška Leischner Fialová^{1,3*}, François Iv⁴, Danièle Salaün¹, Alex Llewellyn⁴, Maxime Gomes⁴, Mayssa Belhabib⁴, Yuxiang Liu⁵, Keisuke Asano⁵, Magda Rodrigues¹, Daniel Isnardon¹, Taro Tachibana^{5,6}, Gijsje H. Koenderink^{2**}, Ali Badache^{1**}, Manos Mavrikis^{4**}, Pascal Verdier-Pinard^{1**}

¹Centre de Recherche en Cancérologie de Marseille (CRCM), INSERM, Institut Paoli-Calmettes, Aix Marseille Univ, CNRS, 13009 Marseille, France

²Department of Bionanoscience, Kavli Institute of Nanoscience Delft, Delft University of Technology, 2629 HZ Delft, The Netherlands

³Department of Pathological Physiology, Faculty of Medicine, Masaryk University, Brno, Czech Republic

⁴Institut Fresnel, CNRS UMR7249, Aix Marseille Univ, Centrale Marseille, 13013 Marseille, France

⁵Department of Bioengineering, Graduate School of Engineering, Osaka City University, Osaka, Japan

⁶Cell Engineering Corporation, Osaka, Japan

*current affiliation: Department of Biology, University of Copenhagen, Copenhagen, Denmark

**Corresponding authors

Keywords: actin/cytoskeleton/microtubule/septin/SEPT9

Abstract

Septins, a family of GTP-binding proteins assembling into higher order structures, interface with the membrane, actin filaments and microtubules, which positions them as important regulators of cytoarchitecture. Septin 9 (SEPT9), which is frequently overexpressed in tumors and mutated in hereditary neuralgic amyotrophy (HNA), mediates the binding of septins to microtubules, but the molecular determinants of this interaction remained uncertain. We demonstrate that a short MAP-like motif unique to SEPT9 isoform 1 (SEPT9_i1) drives septin octamer-microtubule interaction in cells and *in vitro* reconstitutions. Septin-microtubule association requires polymerizable septin octamers harboring SEPT9_i1. Although outside of the MAP-like motif, HNA mutations abrogates this association, identifying a putative regulatory domain. Removal of this domain from SEPT9_i1 sequesters septins on microtubules, promotes microtubule stability and alters actomyosin fiber distribution and tension. Thus, we identify key molecular determinants and potential regulatory roles of septin-microtubule interaction, paving the way to deciphering the mechanisms underlying septin-associated pathologies.

Introduction

Microtubules and actin filaments are cytoskeletal polymers involved in key cellular functions. Microtubules assemble from tubulin dimers to form hollow tubes that have the ability to switch between growing and shortening phases, a process called dynamic instability. Microtubule diversity arises from tubulin isotypes, from post-translational modifications, including acetylation and glutamylation, often associated with stable sub-populations of microtubules, and from associations with specific microtubule-associated proteins (MAPs) that modulate microtubule dynamics (Janke and Magiera, 2020). Microtubules are critically involved in the segregation of chromosomes during cell division and the directed transport of various intracellular cargoes (Carlton et al., 2020). Actin monomers assemble into double helical strands that in cells are often cross-linked into bundles and networks (Maninova et al., 2017). In particular, the presence of associated myosins confers contractility to these actin fiber assemblies, that is essential during both cell division and migration. Such bundled actomyosin fibers form stress fibers that are qualified as peripheral and ventral when running near the cortex and the cell base, respectively. Stress fibers connect focal adhesions and the perinuclear actin cap linked to the top of the nucleus controlling its position and shape (Sneider et al., 2019). Coordinated regulation of the actin and microtubule cytoskeletons, mediated by direct and indirect contacts, is in fact necessary for many biological processes, including cytokinetic furrow positioning, cell migration steering or maturation of neuronal dendritic spines (Dogterom and Koenderink, 2019).

Septins are GTP-binding protein that form heteropolymeric complexes associating with membranes, actin filaments and a subset of microtubules (Woods and Gladfelter, 2020). Like yeast and drosophila septins, human septin hexameric and octameric protomers can polymerize into filaments (Bertin et al., 2012; DeRose et al., 2020; Iv et al., 2021; Ong et al., 2014; Soroor et al., 2021; Szuba et al., 2020; Valadares et al., 2017). Septins function as diffusion barriers for protein compartmentalization and as scaffolds for protein-protein interactions during cell division, and, as evidenced more recently, during interphase (Fung et al., 2014; Marquardt et al., 2019; Mostowy and Cossart, 2012). During cytokinesis, septins are recruited to the sub-membrane cortex by anillin (Oegema et al., 2000; Renshaw et al., 2014) and co-localize with the constricting actomyosin ring, prior to the specification and the maintenance of the ingression furrow position by microtubules (Straight and Field, 2000; Verma and Maresca, 2019). Septins appear also to control abscission (Addi et al., 2018; Estey et al., 2010; Kim et al., 2011; Kinoshita et al., 1997; Renshaw et al., 2014; Surka et al., 2002) that finalizes cell division. It is still unclear how human septins interface with microtubules and the acto-myosin networks. Septins form a collar structure at the neck of dendritic spines, nanotubule-like protrusions and micro-tentacles to guide microtubules (Nolke et al., 2016; Ostevold et al., 2017; Tada et al., 2007; Yadav et al., 2017). In adherent cells, septins concentrate on ventral stress fibers, and less frequently on perinuclear microtubules, depending on the cell type. Despite studies showing that septins regulate the traffic of motor proteins, like kinesin, the binding of MAPs and the guiding of microtubules in polarizing epithelia (Spiliotis, 2010), the functional consequences of septin-microtubule interaction are still largely unknown.

The 13 human septin genes encode four protein sequence homology-groups named after SEPT2, SEPT6, SEPT7 and SEPT3; septins from each group interact with each other in a specific order to form hexamers and octamers (Kim et al., 2011; Sellin et al., 2012; Sirajuddin et al., 2007). Septin octamers differ from hexamers by the addition of septins from the SEPT3 group, with their arrangement recently determined as SEPT2-SEPT6-SEPT7-SEPT3-SEPT3-SEPT7-SEPT6-SEPT2 (Mendonca et al., 2019; Soroor et al., 2021).

Septins include a conserved GTP-binding domain (G domain) flanked by variable N- and C-termini. Septins assemble by the G domain on one side forming the G:G interface and by the N- and C- termini forming the NC:NC interface on the opposite side. This results in (NCSEPT2_{G:G}SEPT6_{NC:NC}SEPT7_{G:G}SEPT7_{NC:NC}SEPT6_{G:G}SEPT2_{NC}) hexamers and (NCSEPT2_{G:G}SEPT6_{NC:NC}SEPT7_{G:G}SEPT3_{NC:NC}SEPT3_{G:G}SEPT7_{NC:NC}SEPT6_{G:G}SEPT2_{NC}) octamers that can polymerize via a universal SEPT2_{NC:NC}SEPT2 interface, that is labile in the presence of high salt concentrations. In the SEPT3 group, SEPT9 has raised most interest because it is ubiquitously expressed, and often overexpressed in tumors (Connolly et al., 2011a). Interestingly SEPT9 is mutated in a large number of hereditary neuralgic amyotrophy (HNA) patients (Collie et al., 2010; Hannibal et al., 2009; Kuhlenbaumer et al., 2005). Alternative splicing resulting in alternative translation start sites gives rise to five SEPT9 isoforms (SEPT9_i1 to_i5) differing by the length and sequence of their N-terminus and by their functions (Connolly et al., 2011b; McIlhatton et al., 2001; Verdier-Pinard et al., 2017). SEPT9_i1, _i2 and _i3 long isoforms share a common structurally disordered N-terminal region (N-ter common to SEPT9 long isoforms) that was proposed, based on *in vitro* studies, to mediate binding to microtubules (Bai et al., 2013). However, several studies indicate that only the isoform 1 of SEPT9 drives the association of septins with microtubules (Nagata et al., 2003; Sellin et al., 2012; Surka et al., 2002; Verdier-Pinard et al., 2017). In order to understand the contribution of septin-microtubule interaction to cell physiology and disease, it is critical to identify and characterize precisely the molecular determinants of this interaction.

In the present study, we show that septin association with microtubules requires a MAP-like motif specific of SEPT9_i1 and the integration of SEPT9_i1 within polymerized septin octamers. *In vitro* reconstitution allowed us to demonstrate a direct and specific interaction of SEPT9_i1-harboring septin octamers with microtubules, which slows down depolymerization of microtubules. Based on this molecular characterization, we designed specific genetic variants, including HNA-like mutations, which modulate SEPT9_i1-microtubule interaction and we show that localizing most of septins on microtubules disturbs stress fiber distribution and tension.

Results

Different SEPT9 isoform expression profiles are associated with distinct octamers/hexamers ratios and cytoskeletal localization. We have analyzed the expression profiles of several septins in commonly used cell models, namely U2OS osteosarcoma, HeLa cervical carcinoma cells, RPE1 retinal epithelial cells and SKBr3 breast carcinoma cells (Fig. 1A). SEPT7 being unique in its group, it is essential for the formation of hexamers and octamers (Fig. S1D). The four cell lines examined expressed very similar levels of SEPT7. In the SEPT2 group, SEPT2 was expressed in all cell lines and SEPT5 was only detected in U2OS cells. Expression of septins from the SEPT6 group was more variable, except for SEPT8 that was expressed at similar levels in all cell lines. U2OS and HeLa cells expressed similar levels of SEPT9. However, U2OS cells expressed mostly isoform 3, whereas HeLa cells expressed mostly isoform 1. RPE1 and SKBr3 cells expressed higher levels of SEPT9 with similar levels of SEPT9_i1 and SEPT9_i2, and no or very low levels of SEPT9_i3.

To assess how SEPT9 expression profiles affected its incorporation in septin hexamers and octamers, we extracted cells in conditions that preserved oligomers and performed native gel electrophoresis and analysis by Western blotting (Fig. 1B and Fig. S1A-D). Based on the detection of the essential SEPT7 and pan-expressed SEPT8, U2OS and HeLa cells contained more hexamers than octamers, as opposed to RPE1 and SKBr3 cells. This result is consistent with higher SEPT9 expression levels in RPE1 and SKBr3 leading to higher levels of

octamers. In addition, our results indicate that long SEPT9 isoforms incorporate indifferently in octamers. We did not detect smaller septin assemblies containing SEPT9 monomers or dimers, suggesting that, at endogenous levels, the entire pool of SEPT9 is stably incorporated into octamers.

Next, we examined the localization of SEPT9 in these cell lines either in interphase or in late cytokinesis (Fig. 1C, D). We observed that SEPT9 was associated with actin fibers in all interphase cells, especially on ventral stress fibers (Fig. 1C, D). Interestingly, consistent with previous observations (Verdier-Pinard et al., 2017), SEPT9 co-localized with a subpopulation of acetylated microtubules in HeLa and SKBr3 cells; in cytokinetic cells, SEPT9 concentrated cortically at the ingression furrow and on the thick bundles of acetylated microtubules contained in the intercellular bridge. In U2OS cells, which express primarily SEPT9_i3, septins associated with the actin cytoskeleton but did not co-localize with microtubules. These results indicate that the association of septins with microtubules is dependent on the presence of octamers harboring SEPT9_i1, in agreement with observations by others (Nagata et al., 2003; Sellin et al., 2012; Surka et al., 2002). It is less clear why in RPE1 cells, despite SEPT9_i1 levels comparable to those in SKBr3 cells, there was no association of SEPT9 with microtubules, except in primary cilia (Fig. 1E).

SEPT9_i1 interacts with microtubules via a specific MAP-like motif. The fact that SEPT9_i1, but not the closely related i2 and i3 isoforms, is required for septins to bind microtubules identifies the sequence formed by the first specific 25 amino acid residues of the SEPT9_i1, as key for its interaction with microtubules (Verdier-Pinard et al., 2017). The fact that the sequence is well conserved in all classes of vertebrates (Fig. S2) is also indicative of an important function. A search for similar sequences in proteins related to the microtubule cytoskeleton by using the NCBI Blastp tool identified the Arabidopsis thaliana AIR9 protein, a plant MAP involved in cytokinesis (Buschmann et al., 2006). Sequence alignments showed that a sequence (AIR9 173-205) located in the AIR9-microtubule binding domain (AIR9 1-234) (Buschmann et al., 2006) was homologous to SEPT9_i1 specific sequence identifying an AIR-9-like block (Fig. 2A). Another sequence in the AIR9 N-terminus (amino acids 46-78) presented some similarities with the SEPT9_i1 specific sequence (Fig. 2A). Strikingly, the AIR9-like block had similarities with canonical repeats found in the microtubule binding domains (MBDs) of the structural human MAPs MAPT (tau), MAP2 and MAP4, which are known to interact directly with the surface of microtubules (Fig. 2A). An N-terminal small block in the SEPT9_i1 specific sequence showed similarities with the MAP4 R2 repeat. Thus, SEPT9_i1 displays a putative MBD, similar to the MBD repeats of several MAPs, constituted by a MAP4 R2-like sequence followed by an AIR9-like sequence.

To unequivocally demonstrate that this motif is actually the MBD of SEPT9_i1, we examined the localization of SEPT9_i1 mutants (C-terminally tagged with GFP) presenting deletions or point mutations in the first 25 amino acid residues (Fig. 2B), expressed in U2OS cells (Fig. 2C, D and Fig. S3A-C). U2OS cells were chosen because they express very low levels of SEPT9_i1 (Fig. 1A), and show no SEPT9-microtubule co-localization (Fig. 1C, D). In addition, U2OS cells were amenable to simultaneous siRNA-mediated knockdown (KD) of SEPT9 and expression of exogenous SEPT9_i1-GFP constructs at near-endogenous SEPT9 levels (Fig. S3A). Wild type SEPT9_i1 co-localized with actin in all cells and with microtubules in more than 60% of the cells. SEPT9_i3 and the Δ 1-25 SEPT9_i1 mutant also associated with actin fibers, but never localized to microtubules (Fig. 2C, D, F, H and Fig. S3B, D). This result is consistent with our previous observations in SKBr3 cells (using N-terminally GFP-tagged constructs) (Verdier-Pinard et al., 2017). Deletion of the AIR9-like portion (Δ 10-25 mutant) or of the MAP4 R2-like portion (Δ 1-7 mutant) totally or largely abrogated SEPT9 binding to microtubules, respectively (Fig. 2C and Fig. S3B). Next, we

introduced point mutations in the AIR9-like portion (Fig. 2B). Independent mutations of two sets of contiguous serine residues (S12A/S13A and S22A/S23A), conserved in the AIR9 MBD, did not significantly alter the proportion of cells showing co-localization of SEPT9 with microtubules (Fig. 2C, D and Fig. S3B, C). Importantly, upon mutations of the two arginine residues (R10A/R15A), conserved in all vertebrates (Fig. S2) and present in the AIR9 MBD, the population of cells showing the SEPT9 binding to microtubules was abrogated (Fig. 2C, D and Fig. S3B, C). In another set of experiments, we evaluated the impact of mutations of the SEPT9_i1 putative MBD on the extent of SEPT9_i1 co-localization with microtubules and actin fibers in individual cells, through intensity correlation coefficient-based image analysis (Bolte and Cordelières, 2006). This analysis confirmed that deletion of SEPT9_i1 specific sequence or R10A/R15A mutations strongly diminished the extent of co-localization of SEPT9_i1 with microtubules, while promoting co-localization with actin fibers (Fig. S4A). In addition, this analysis revealed that S12A/S13A mutations strongly promoted the extent of SEPT9_i1 co-localization with microtubules (Fig. S4A). Collectively, our data show that the SEPT9_i1 specific N-terminal sequence is an MBD analogous to the ones found in human MAPs and the plant AIR9 MAP. Of note, in contrast to MAP MBDs, the SEPT9_i1 specific sequence is not tandem-repeated and lacks upstream conserved residues (Fig. 2A).

A previous report proposed, based on *in vitro* studies using recombinant polypeptides, that SEPT9_i1₆₁₋₁₁₃ within the N-ter common to SEPT9 long isoforms was the main contributor to microtubule binding (Bai et al., 2013). To evaluate a potential contribution of the N-ter common to SEPT9 long isoforms, we generated a chimeric SEPT9 deleted of this entire region, fusing the isoform 1 specific sequence to SEPT9_i5, the shortest SEPT9 isoform, and named it SEPT9_i1-i5 (Fig. 2E). Whereas SEPT9_i5 localized strictly to actin fibers (Fig. 2F, H and Fig. S3E), fusion to the SEPT9_i1 specific motif was sufficient to localize septins to microtubules in all interphase cells (Fig. 2F, H). Surprisingly, this was accompanied by the complete loss of SEPT9 co-localization with actin fibers (Fig. 2F, H). Consistent with these findings, expression of SEPT9_i1-i5 during cytokinesis strongly increased the percentage of cells showing SEPT9 association with microtubule bundles at the intercellular bridge (Fig. S3D).

Our results demonstrate that the SEPT9_i1 MBD is required and sufficient to target SEPT9 to microtubules, whereas the N-ter common to SEPT9 long isoforms is dispensable. Interestingly the SEPT9_i1-i5 is much more efficient than SEPT9_i1 for targeting septins to microtubules (Fig. 2C, F and Fig. S3B, D), hinting that the N-ter common to SEPT9 long isoforms might have a negative regulatory function. Septin 9 gene mutations in HNA patients are located in the N-ter common to SEPT9 long isoforms (Kuhlenbaumer et al., 2005), but their impact on SEPT9 function remains to be elucidated. We introduced separately the two most frequently described HNA mutations (R106W and S111F) in SEPT9_i1 constructs and evaluated their impact on SEPT9_i1 localization. Both SEPT9_i1 R106W and S111F maintained co-localization with ventral stress fibers (Fig. 2G, H). However, both mutations impaired the association with microtubules (Fig. 2G, H). This result confirms that the N-ter common to SEPT9 long isoforms, while not required for SEPT9 microtubule binding per se, is an important regulatory domain and provides novel insights into the molecular etiology of HNA.

SEPT9_i1 must be included in a polymerized septin octamer to associate with microtubules. In contrast to typical MBDs in structural MAPs, the SEPT9_i1 specific sequence does not have tandem repetitions. We hypothesized that the dimerization of SEPT9_i1 in octamers via the NC interface brings two SEPT9_i1 specific sequences in close proximity, mimicking MBD tandem arrangements of repeats. To test this hypothesis, we

introduced point mutations into SEPT9_i1 that should disturb the NC interface and generate tetramers; and to more generally assess the oligomeric environment required for microtubule binding, we introduced point mutations in the G interface to generate non-incorporated SEPT9_i1 (Sirajuddin et al., 2007) (Fig. 3A and Fig. S5A). We then expressed these constructs in U2OS cells in place of endogenous SEPT9 (knocked down via siRNA). Importantly, re-expression of wild type SEPT9_i1-GFP restored close to endogenous levels of octamers and hexamers (Fig. 3A and Fig. S5A). As expected, most of the SEPT9_i1 G interface mutant (SEPT9_i1 G_{mut}) did not incorporate in octamers (Fig. 3A and Fig. S5A). Instead, it migrated with an apparent molecular weight of 138 kDa, corresponding most likely to monomeric SEPT9_i1, whose gel motility is retarded by the long and disordered N-terminus (Sellin et al., 2012) (Fig. S1A and Fig. S1E). Based on previous studies (Bertin et al., 2010; Kim et al., 2011; Sirajuddin et al., 2007), we generated two SEPT9_i1 NC interface mutants with mutations in the $\alpha 0$ helix either in the basic residue stretch (SEPT9_i1 NC_{mut1}) or upstream of this stretch in key hydrophobic residues (SEPT9_i1 NC_{mut2}). SEPT9_i1 NC_{mut1} incorporated in tetramers and SEPT9_i1 NC_{mut2} incorporated partly in tetramers, but mostly migrated like the monomeric protein (Fig. 3A and Fig. S5A), indicating that mutations in SEPT9_i1 NC_{mut2} might affect both NC and G interfaces. Importantly, we observed no association of SEPT9_i1 G or NC mutants with microtubules, but rather a diffuse cytosolic distribution (Fig. 3B). These results show that neither septin tetramers nor SEPT9_i1 monomers bind to microtubules, and that the octameric septin context, which brings together two SEPT9 units via their NC interface, is mandatory for SEPT9_i1 association with microtubules. Of note, SEPT7 was still incorporated in hexamers when G or NC SEPT9 interfaces were altered (Fig. S5A), but was detected in scattered undefined locations in cells (Fig. S5B).

Next, we evaluated if septin octamers harboring SEPT9_i1 bind microtubules by themselves or if they need to assemble into longer polymers via SEPT2:SEPT2 NC interfaces. Mutation of the SEPT2 NC interface (Kim et al., 2012; Sirajuddin et al., 2007) (SEPT2 NC_{mut}) should produce a mixture of isolated octamers and hexamers in cells (Fig. 3C). To evaluate its impact on SEPT9_i1 localization, we knocked down both SEPT9 and SEPT2, and re-expressed SEPT9_i1 (tagged with GFP to monitor SEPT9 localization), together with wild type SEPT2 or SEPT2 NC_{mut} (tagged with mApple to identify transfected cells). Using native gel separation, we verified that wild type SEPT2 and SEPT2 NC_{mut} generated the same relative expression levels of octamers and hexamers (Fig. 3C). However, when SEPT2 NC_{mut} was expressed, septins no longer co-localized with microtubules (Fig. 3D). Thus, the association of septins with microtubules requires incorporation of SEPT9_i1 in polymerizable octamers.

SEPT9_i1 associates with stable microtubules. Because of the sequence similarities between SEPT9_i1 and MAP4 MBDs, the two proteins might use the same tubulin interdimer binding pocket at the surface of microtubules (Kellogg et al., 2018; Shigematsu et al., 2018). In SKBr3 cells, which express endogenous SEPT9_i1, we observed that MAP4 associated with the entire microtubule cytoskeleton, whereas septins (using SEPT7 as readout) was concentrated on acetylated bundled microtubules (Fig. 4A). In U2OS cells transfected with SEPT9_i1, the same differential distribution between MAP4 and SEPT9_i1 (or SEPT9_i1-i5) was observed (Fig. 4B). Upon closer inspection of MAP4 and SEPT9_i1/SEPT9_i1-i5 co-alignment with microtubule bundles, we observed the preferential association of SEPT9 with microtubule bundles located towards the center of the cell near the nucleus (at the expense of MAP4) and the preferential association of MAP4 on peripheral microtubule bundles (at the expense of SEPT9) (Fig. S6). This apparent competition between SEPT9_i1 and MAP4 for

association with microtubules suggests that the binding sites of SEPT9_i1 MBD and MAP repeats partially overlap on the microtubule lattice.

We repeatedly observed the preference of SEPT9_i1 for acetylated microtubules (Fig. 1D, E, Fig. 2D, H, Fig. 3B, D, Fig. 4A and Fig. S3C), suggesting that microtubule acetylation could be a determinant of septin binding. Moreover, when comparing the two retina epithelial cell lines, RPE1 and ARPE19 which expressed similar levels of SEPT9_i1 (Fig. 5A), we observed that tubulin acetylation levels were low in RPE1 and high in ARPE19, correlating with the ability to associate with microtubules (Fig. 5B, Fig. S3F). Other posttranslational modifications (PTMs) of tubulins, such as polyglutamylation, that could affect SEPT9_i1 binding (Froidevaux-Klipfel et al., 2015; Spiliotis et al., 2008) were equally low in these cell lines (Fig. 5A). Actually, treating RPE1 cells with paclitaxel, a drug that induces acetylation and bundling of microtubules in cells, induced the association of septins with microtubules (Fig. 5C). Thus, SEPT9_i1 association with microtubules appeared to be correlated with tubulin acetylation. Of note, the paclitaxel-driven re-localization of septins to microtubules was clearly dependent on the expression of SEPT9_i1, irrespective of the cell line in which it was expressed (Fig. 4C, Fig. 5C and Fig. S4B). To determine if paclitaxel-induced tubulin acetylation was responsible for re-localization of septins on microtubules, α TAT1, the major tubulin acetyl transferase (Janke and Montagnac, 2017), was knocked down to prevent tubulin acetylation, prior to paclitaxel treatment (Fig. 5D). This experiment clearly showed that re-localization of septins on paclitaxel-bundled microtubules was independent of tubulin acetylation levels (Fig. 5D).

Finally, we evaluated whether SEPT9_i1, like MAPs, contributed to stabilizing microtubules in the presence of microtubule-depolymerizing agents, such as nocodazole. We observed that, whereas SEPT9_i1 moderately stabilized microtubules, SEPT9_i1-i5 strongly promoted the resistance of microtubules against nocodazole-induced depolymerization (Fig. 4C, D and Fig. S3G). Of note, depolymerization of microtubules allowed SEPT9_i1-i5 to re-localize to actin fibers in nearly 60% of the cells (Fig. 4C). These results are reminiscent of the strong microtubule stabilizing effect against nocodazole-induced depolymerization induced by the expression of MAP4 mutants that bound microtubules more avidly (Chang et al., 2001). Collectively, these data establish that septin octamers harboring SEPT9_i1 associate with a population of stable bundled microtubules in cells, independently of their acetylation levels, and contribute to microtubule stabilization.

Recombinant septin octamers harboring SEPT9_i1 interact directly and specifically with microtubules and slow down their depolymerization. In order to assess if recombinant octamers harboring SEPT9_i1 are able to bind directly and specifically to microtubules, we purified recombinant septin octamers harboring either SEPT9_i1 (Oct_9i1: SEPT2-SEPT6-SEPT7-SEPT9_i1-SEPT9_i1-SEPT7-SEPT6-SEPT2) or SEPT9_i3 (Oct_9i3: SEPT2-SEPT6-SEPT7-SEPT9_i3-SEPT9_i3-SEPT7-SEPT6-SEPT2) (Iv et al., 2021) (Fig. S1B) and reconstituted dynamic microtubules made from purified tubulin α/β -heterodimers in the presence of each type of octamer. Total internal reflection fluorescence (TIRF) microscopy allowed visualizing both dynamic microtubules incorporating rhodamine-tagged tubulin and septin oligomers incorporating GFP-tagged SEPT2 (Fig. 6A). Microtubules were polymerized from a 10 μ M tubulin heterodimer solution and in the presence of 10 to 300 nM of octamers, i.e. at concentrations comparable to the tubulin α/β -heterodimer (\sim 10 μ M) and septin complex (\sim 400 nM) concentrations measured in Hela cells (Hein et al., 2015).

We clearly observed Oct_9i1 binding to microtubules at the lowest concentration (10 nM, Fig. 6B, C). Oct_9i1 diffused randomly on the lattice of dynamic microtubules (Fig. 6C and Movie 1), and were also present on the stable microtubule seeds. On kymographs, the diffusion of Oct_9i1 on microtubules during the growing phases was clearly apparent (Fig.

6C). At 10 nM concentration, there were no detectable recombinant octamers harboring SEPT9_i3 (Oct_9i3) on dynamic or stable seed microtubules. Decoration of microtubules increased with increasing concentrations of Oct_9i1, until saturation at 300 nM (Fig. 6B, C and Movie 1). In comparison, Oct_9i3 only showed significant binding at the highest concentration (300 nM); Oct_9i3 binding was restricted to the stable microtubule seeds (Fig. 6B, C and Movie 2). Altogether these results show that octamers harboring SEPT9_i1 bind specifically and directly dynamic individual microtubules.

We then analyzed how the addition of Oct_9i1 or Oct_9i3, at 10 to 300 nM, affected parameters of microtubule dynamic instability (Fig. 7A, B and Table S1). Both types of octamer were similarly and moderately affecting microtubule growth rate at intermediate concentrations. Strikingly, Oct_9i1 induced a strong and dose-dependent decrease of the microtubule shortening rate, while Oct_9i3 had no effect, even when used at the highest concentration. The catastrophe rate was not consistently altered by the addition of either types of octamer. Intriguingly, we observed that, in the presence of 200 to 300 nM of Oct_9i1, about 10% of depolymerizing microtubules formed at their plus-end an unusual, curved tubulin-containing structure that was decorated by septins (Fig. 7C and Movie 3).

Finally, we assessed the impact of the N-ter region common to SEPT9 long isoforms on octamers microtubule binding and regulation of microtubule dynamics *in vitro*, using recombinant octamers harboring SEPT9_i1-i5 (Oct_9i1-i5) (Fig. 7, Movie 4). Strikingly, at 10 nM, Oct_9i1-i5 septin fully covered the microtubules (Fig. S7A, Movie 4), in strong contrast to sparse binding of the microtubule lattice exhibited by Oct_9i1 at the same concentration (Fig. 6, Movie 1). We also observed that at 10 nM, Oct_9i1-i5 reduced the shortening rate to the same extent than 75-100 nM of Oct_9i1 (Fig. S7B, Table S2 and Fig. 7). Thus, consistent with observations in cells, the N-ter common to SEPT9 long isoforms was dispensable for septin octamers microtubule binding and negatively affected this interaction. In addition, at 50 nM, the Oct_9i1-i5 frequently rescued shortening microtubules and at 100 nM, some microtubules displayed continuous growth, stopped growing and remain stable (Fig. S7C). These *in vitro* observations are consistent with the stabilization of microtubules upon the expression of SEPT9_i1-i5 in cells (Fig. 4D and Fig. S3G). Surprisingly, at 300 nM, Oct_9i1-i5 almost completely prevented microtubule growth altogether (Fig. S7C) and caused formation of stable loops at microtubule plus-ends (Fig. S7A). These results confirm that the N-ter common to SEPT9 long isoforms plays an important regulatory role on septin-microtubule interaction.

Re-localization of octamers from stress fibers to microtubules alters stress fiber organization and function.

Our observations indicate that the population SEPT9_i1 octamers associates with both microtubules and actin fibers and can shuttle between them. This was for instance illustrated by the observation that the SEPT9_i1-i5 chimera co-localized with microtubules only (Fig. 2F, H and Fig. 4B, C), but was able to co-localize with actin fibers upon nocodazole-induced depolymerization of microtubules (Fig. 4C). Thus, beyond its direct contribution to microtubule stability and dynamics (this study) and microtubule-linked processes, e.g. cell resistance to paclitaxel (Targa et al., 2019), the relative distribution of SEPT9_i1 on microtubules vs. actin fibers might indirectly affect actomyosin fibers distribution or properties. Previous studies showed that SEPT9 associated with perinuclear actin fibers, especially ventral stress fibers whose organization depended on SEPT9 (Farrugia et al., 2020; Verdier-Pinard et al., 2017). We similarly observed that in U2OS (Fig. 8A) and RPE1 cells (Fig. S8B-D), the knockdown of SEPT9 strongly decreased the percentage of cells with sub-nuclear stress fibers. To test the hypothesis that septin octamer association with microtubules might impact actin fiber organization and function, we generated U2OS cell lines stably

expressing SEPT9_i1 wt or mutants (Fig. S8E), which recapitulated the relative distribution of SEPT9_i1 on microtubules vs. actin fibers observed upon transient transfection (Fig. S8F, Fig. 2C and F)

Expression of SEPT9_i1-i5, that only associated with microtubules, was concomitant with a strong reduction in the percentage of cells having sub-nuclear stress fibers (Fig. 8B), while expression of SEPT9 constructs with no or reduced microtubule association (SEPT9_i1 Δ 1-25, SEPT9_i1 R10A/R15A and SEPT9_i3) preserved sub-nuclear stress fibers (Fig. 8B). Likewise, paclitaxel-induced re-localization of SEPT9_i1 octamers from stress fibers to microtubule bundles in RPE1 cells induced the loss of sub-nuclear stress fibers (Fig. 5C), whereas paclitaxel-treatment of U2OS, which express SEPT9_i3 as the major isoform, did not affect sub-nuclear stress fibers (Fig. 5C). Thus, the sequestration of septin octamers on microtubules, which is dependent on the MBD of SEPT9_i1, induces a loss of sub-nuclear stress fibers, suggesting that the precise relative distribution of septins on microtubules vs. actin fibers is critical for the actin cytoskeleton organization, which is coherent with observations by others (Calvo et al., 2015; Kinoshita et al., 2002; Targa et al., 2019).

To further assay the interplay between SEPT9_i1-microtubule association and stress fiber function, we plated U2OS cells knocked down for SEPT9 or expressing SEPT9_i1 wt or mutants on adhesive micropatterns (Fig. 8C). Indeed, when plated on adhesive micropatterns, cells form actin stress fibers across adhesives edges, and the convexity of the non-adhesive cell edges provides a readout for stress fiber tension (Thery et al., 2006). Partial or total relocalization of septins on microtubules in U2OS cells stably expressing SEPT9_i1 or SEPT9_i1-i5 respectively, promoted the concavity of non-adhesive cell edges, reflective of the relaxation of peripheral stress fibers compared to cells stably expressing SEPT9_i1 Δ 1-25, that is solely located on actin fibers (Fig. 8C). The knockdown of SEPT9 in U2OS cells, leading to the loss of septin octamers, induced a similar detectable relaxation of peripheral stress fiber (Fig. 8D).

Altogether, these results suggest that the relative abundance of octamers vs. hexamers and the relative proportion of septin octamers able to associate to microtubules critically affect the actomyosin organization and tension.

Discussion

Earlier studies have shown that SEPT9_1 has a preferential affinity for microtubules in cells (Nagata et al., 2003; Sellin et al., 2012; Surka et al., 2002; Verdier-Pinard et al., 2017) indicating that the first 25 amino acid residues defining the sequence unique to this long isoform was responsible for specific binding to microtubules. In the present study, we identify a conserved MAP-like MBD in SEPT9_i1, including two distinct modules and key conserved residues whose mutation modulates microtubule binding. We and others had identified imperfect repeats containing basic amino acid residues in the common N-terminal sequence of SEPT9_i1, _i2 and _i3 (Bai et al., 2013; Verdier-Pinard et al., 2017). These repeats were proposed to constitute the MBD of SEPT9 via electrostatic interactions with the acidic C-termini of β -tubulin exposed at the surface of microtubules (Bai et al., 2013), in line with the accepted mode of interaction of conventional MAPs at the time (Serrano et al., 1985). However, recent advances in the determination of the structure of MAP tandem repeats bound to microtubules by cryo-EM contradict this model (Kellogg et al., 2018; Shigematsu et al., 2018). These studies reveal that a sequence in MAPT and MAP4 repeats anchors MAPs to a binding pocket at the interface between consecutive tubulin heterodimers in protofilaments, independently of tubulin acidic C-termini. We actually found numerous similarities between MAPs repeated sequences and the SEPT9_i1 MBD, that are not present in the imperfect

repeats shared with the other SEPT9 long isoforms. Most importantly, our data show that, contrary to the SEPT9_i1 MBD, the N-ter common to SEPT9 long isoforms is not required for the association of SEPT9_i1 harboring octamers with microtubules. Deletion of this region actually enhanced septin association with microtubules. These findings led us to speculate that the N-ter common to SEPT9 long isoforms is not directly involved in the interaction of SEPT9_i1 with the microtubule lattice, but negatively regulates it. The imperfect repeats in the N-ter common to SEPT9 long isoforms were predicted to form short β -sheets (Verdier-Pinard et al., 2017). One of these imperfect repeats is the locus of mutations detected in HNA patients (Collie et al., 2010; Hannibal et al., 2009; Kuhlenbaumer et al., 2005). Thus, it is possible that these predicted ordered regions generate a folding that places the SEPT9_i1 MBD favorably for its binding to the surface of microtubules. Consistent with this hypothesis, structure prediction of the long N-terminus of SEPT9_i1 using Raptor X Contact Predict, a server with an algorithm powered by deep learning (Xu et al., 2021), confirms that the region harboring these imperfect repeats is folded, whereas the rest of the N-terminus is mostly disordered (Fig. S1E). In addition, RaptorX Property, a tool predicting structure property of a protein sequence without using any templates (Wang et al., 2016), confirmed that the imperfect repeat harboring HNA mutations could form a β -sheet and constitute a unique strongly ordered micro-domain; this β -sheet is predicted in several models generated by RaptorX Contact predict to associate antiparallel with a β -sheet starting right after the SEPT9_i1 MBD (Fig. S1E) (Verdier-Pinard et al., 2017). Such folding would increase the proximity of the SEPT9_i1 MBD with the octamer, reducing its wandering. Disturbance of this folding could induce an increase in the degree of freedom of the SEPT9_i1 MBD that is less favorable for its binding on the microtubule lattice. Indeed, generating maximal proximity between the SEPT9_i1 MBD and the octamer via the deletion of the N-ter common to SEPT9 long isoforms (SEPT9_i1-i5) strongly promoted microtubule binding and stability. Remarkably, when we expressed SEPT9_i1 harboring HNA-like mutations, septin octamers were no longer able to associate with microtubules, while still associating with actin fibers, suggesting that HNA mutations alter the putative “SEPT9_i1 MBD regulatory region” and providing clues for the determination of the molecular mechanisms underlying HNA. In addition, the conformational status of this folded region could be regulated by PTMs. Indeed, it was proposed that phosphorylation of the first threonine residue after the SEPT9_i1 MBD (Thr38 in SEPT9_i1, Thr24 in SEPT9_i3) by Cdk1 during mitosis induces a conformational change of the SEPT9 N-terminus via the action of Pin1 on the adjacent proline residue (Pro39 and Pro25 in SEPT9_i1 and _i3, respectively) (Estey et al., 2013). Further investigations identifying PTM regulations in relation to the N-terminus conformation of SEPT9 long isoforms will be necessary.

Importantly, we demonstrated that SEPT9_i1 localizes septins on microtubules, only if it is included in polymerizable septin octamers. At endogenous expression levels, in the diverse cellular models we studied, we did not observe the presence of a significant pool of monomeric SEPT9 (Fig. 1B), which suggests that microtubule-associated SEPT9 is wholly incorporated in octamers in these cells. Conversely, the large excess of SEPT9_i1 monomers in cells expressing the SEPT9_i1 G interface mutant was not associated with microtubules (Fig. 3A, B). Thus, *in vitro* studies with isolated recombinant SEPT9_i1 suggesting that SEPT9_i1 can binds and bundle microtubules by itself (Bai et al., 2013; Karasmanis et al., 2018; Nakos et al., 2019b) must be interpreted with caution.

In previous studies, recombinant SEPT9_i3, or the N-ter fragments located in the N-ter common to SEPT9 long isoforms, were shown to associate with microtubules, assembled from purified tubulin (Bai et al., 2013; Nakos et al., 2019b). The discrepancy is most likely linked to the fact that in these *in vitro* experiments, SEPT9 was used outside of its natural octameric context, often at high concentrations (up to 10-30 μ M in pelleting assays) and using

paclitaxel or GMPCPP stabilized microtubules in very low salt buffers, which likely favored electrostatic interactions. Using recombinant octamers harboring SEPT9_i1 and SEPT9_i3, we observed that only those harboring SEPT9_i1 associated with dynamics microtubules at low nanomolar concentrations, *in vitro*. Our *in vitro* reconstitution experiments results are the first one to recapitulate the specific binding of SEPT9_i1 octamers to microtubules observed in cells. Of note, although recombinant SEPT2-SEPT6-SEPT7-SEPT7-SEPT6-SEPT2 hexamers were found to interact with microtubules *in vitro* (Nakos et al., 2019a), this is not consistent with the absence of co-localization of septin hexamers with microtubules, when SEPT9 was knocked down in cells (Fig 8A and Fig. S1D) (Verdier-Pinard et al., 2017).

Septins associate with a sub-population of bundled microtubules (Bai et al., 2013; Bowen et al., 2011; Nagata et al., 2003). We confirm that SEPT9_i1 co-localize with acetylated, bundled microtubules (much more selectively than structural MAPs, such as MAP4). As we show also that microtubule acetylation is not a requirement, SEPT9_i1 binding appears rather to rely on microtubule bundling in cells. Intriguingly, microtubule bundling is not required *in vitro*. This paradox will require other studies, including structural approaches, to further characterize the molecular bases of the association of septins with individual and bundled microtubules.

Our data show that octamers harboring SEPT9_i1 slowed down microtubule depolymerization *in vitro* and stabilized microtubules in cells treated with nocodazole. It will be important to determine how these molecular events contribute to microtubule-dependent cellular processes such as spatiotemporal sorting of vesicles and organelles (Karasmanis et al., 2018; Spiliotis et al., 2008), formation of protrusive structures (Ghossoub et al., 2013; Hu et al., 2012; Nolke et al., 2016; Ostevold et al., 2017; Tada et al., 2007; Yadav et al., 2017) or cell survival against cytotoxic doses of paclitaxel (Targa et al., 2019).

Association of septins with microtubules is likely to be regulated by cell- and tissue-specific contexts. Indeed, septin association with microtubules is clearly correlated to the specific expression of the SEPT9_i1 isoform and is sensitive to the bundling state of microtubules. Septin-microtubule interaction might also be modulated by the presence of competing MAPs or PTMs targeting the SEPT9_i1 MBD and/or its putative regulatory domain. HNA-associated defects might be related to dysregulated microtubule function, or to an excessive association of septins with actin fibers and perturbation of actomyosin functions. Our work presents new molecular basis for studying the physiological relevance of the association of septin with microtubules, and opens new avenues in the difficult search for the causative events leading to this rare neuropathy.

Materials and methods

Human Cell lines.

U2OS (ATCC), SKBR-3 (ATCC), HeLa (a kind gift from Dr Patrice Dubreuil, CRCM, Marseille, France), RPE-1 and ARPE19 (kind gifts from Dr Michael Sebbagh, CRCM, Marseille) cells were maintained in Dulbecco's modified Eagle's medium (DMEM) (Gibco) supplemented with 4 mM GlutaMAXTM, 10 % fetal bovine serum (FBS) and 1% sodium pyruvate (supplemented DMEM), except ARPE19 cells that were cultivated in DMEM/F12 (1:1 mixture of DMEM and Ham's F12, Gibco) supplemented as for DMEM. All cell lines were maintained in the presence of 5% CO₂ humidified atmosphere at 37°C. RPE-1 cells were also grown on coverslips coated with collagen (Corning, Cat#354236) until they reached confluency and ciliogenesis was induced by growing cells in DMEM containing only 0.5% of fetal bovine serum for 24 hours. Cells were tested negative for mycoplasma and have not been authenticated recently.

Plasmids coding for fluorescent septin constructs and transfection

To drive expression of the constructs in mammalian cells, we used the immediate early enhancer and promoter of human cytomegalovirus (CMV promoter, 508 base pairs). Human SEPT9_i1 cDNA was a gift from C. Montagna (Albert Einstein College of Medicine, USA). Human SEPT9_i3 cDNA was a gift from W. Trimble (University of Toronto, Canada). A synthetic human SEPT2 coding sequence (Eurofins Genomics, Germany) was generated using the codon usage of mouse SEPT2 except for the five codons that differ between the two species, for which we used codons encoding the human residues. C-terminal green and red fluorescent protein fusions were generated using monomeric (V206K) superfolder GFP (msfGFP) (Costantini et al., 2012; Cranfill et al., 2016; Pedelacq et al., 2006; Zacharias et al., 2002) and monomeric Apple (mApple) (Cranfill et al., 2016; Shaner et al., 2008), respectively. All constructs were generated with two-insert seamless cloning (In-Fusion HD Cloning Plus Kit from Takara Bio, Cat# 638910) using NheI/BamHI linearized plasmid backbones (Addgene plasmid #54759) and the oligonucleotide primer sequences (listed in Table S2). Primers for seamless cloning were Cloning Oligo (<60 bp) or EXTREmer (>60 bp) synthesis and purification quality from Eurofins Genomics, Germany. Restriction enzymes were FastDigest enzymes from Thermo Scientific. All plasmids were verified by sequencing (Eurofins Genomics, Germany) after each cloning step, including the midipreps used for plasmid production. Constructs (3 µg) were transiently transfected by nucleofection in cells with Cell line Nucleofector kit V and using Amaxa nucleofector program U2OS X-001 and T47D X-005 for U2OS and SKBr3 cells, respectively, following manufacturer instructions (Lonza), and cells were cultured for 72 h after transfection and either fixed or extracted for proteins to perform immunocytochemical or biochemical analyses, respectively.

siRNAs and transfection

The following 19-mer duplex siRNAs were purchased from LifeTechnologies: siRNA control (siCtrl) targeting the E.Coli β galactosidase (LacZ) (5'-GCGGCUGCCGGAUUAUACC-3'), SEPT9 (5'-GGAUCUGAUUGAGGAUAAA-3') targeting the 3'UTR of all human SEPT9 mRNA variants, SEPT7 (5'-CGACUACAUUGAUAGUAAA-3') targeting the human mRNA coding region, αTAT1 (5'-CGCACCAACUGGCAAUUGA-3'), whose design was based on validated siRNA αTAT1#2 from Shida et al (Shida et al., 2010). Transfection of 200 or 134 picomoles of siRNA was performed with Lipofectamine RNAiMAX (Invitrogen, Cat# 13778075) or Amaxa cell line nucleofection kit V (Lonza, Cat#VCA-1003) following manufacturer instructions, respectively. Cells were cultured for 72 h after transfection and either fixed or extracted for proteins to perform immunocytochemical or biochemical analyses, respectively.

Drug treatments

For some experiments, cells were treated for two hours with 2 µM paclitaxel (Sigma-Aldrich, Cat#T7191) or 10 µM nocodazole (Sigma-Aldrich, Cat#M1404) in DMSO or with DMSO alone (Sigma-Aldrich, Cat#D8418).

Antibodies

Labeling of septins on Western blots (WB) and/or on immunocytochemistry coverslip (ICC) was achieved with the following antibodies: rabbit polyclonals against human SEPT2 (Sigma-Aldrich, Cat#HPA018481, WB), against human SEPT9 (Sigma-Aldrich, Cat#HPA042564 and HPA050627, WB and ICC; Proteintech, Cat#10769-1-AP, WB), against Septin 7 (IBL, cat#18991, WB and ICC), against SEPT11 (Sigma-Aldrich, Cat#SAB2102111, WB), against human SEPT5, against SEPT8 (kind gifts from Barbara Zieger, University of Freiburg, Germany, WB), against SEPT6 (a kind gift from Makoto Kinoshita (Nagoya University,

Japan, WB), against Sept10 (Sigma, Cat#HPA047860, WB); rat monoclonals against human SEPT9_i1 (clone 4D2A5, WB) or human SEPT9_i3 (clone 1A6C2, WB), and against human SEPT7 (clone 10A7, WB and ICC) were produced as described previously (Verdier-Pinard et al., 2017) (WB). Other antibodies were against α -tubulin: mouse monoclonal (Sigma-Aldrich, DM1A Cat#05-829, WB and ICC), rat monoclonal (Invitrogen, YL1/2 Cat#MA1-80017, ICC), mouse monoclonal anti-acetylated K40 (Santa Cruz Biotechnology, 6-11B1 Cat#sc-23950, WB and ICC), against tubulin: mouse monoclonal anti-glutamylated tubulin (Adipogen, GT-335 Cat#AG-20B-0020-C100 and polyE Cat#AG-25B-0030-C050, WB). Labeling of actin was performed with phalloidin-Atto 390 (Sigma-Aldrich, Cat#50556, ICC) or phalloidin-TRITC (Sigma-Aldrich, Cat#P1951, ICC). Secondary antibodies conjugated with HRP were used for WB (Dako Agilent). For ICC application, and for WB application when indicated in figures, the following fluorophores conjugated to secondary antibodies were used: DYLIGHT405, AlexaFluor405, AlexaFluor488 and AlexaFluor594 (Jackson, ImmunoResearch) and AlexaFluor 647 (Invitrogen).

U2OS cell lines stably co-expressing mCherry-H2B and SEPT9-GFP constructs

U2OS and HeLa cell lines stably expressing mCherry-H2B and a SEPT9_X-GFP construct were generated by co-transfecting the plasmid pBabeD hygro mCherry-Histone H2B (a kind gift from Christophe Lachaud, CRCM, Marseille, France) with hygromycin B resistance and one of the plasmids encoding for different SEPT9 isoforms and mutants-GFP constructs, with geneticin resistance. U2OS cells were nucleo-transfected (Amaxa nucleofactor program U2OS X-001, Lonza) with Amaxa kit V. Three days after transfection, co-expressing cells were selected with hygromycin B (Invitrogen, Cat#10687-010) and geneticin (Gibco, Cat#10131-027) at 0.5 mg/mL each. GFP and mCherry fluorescence positive cells were sorted by flow cytometry. Sorted cell populations were cultured in supplemented DMEM in the presence of 0.5 mg/mL of antibiotics. After three passages, cell line stocks were stored in liquid nitrogen.

Micropatterning of U2OS cells

6×10^3 U2OS cells KD for SEPT7 or SEPT9 or U2OS cells stably co-expressing mCherry-H2B and SEPT9-GFP constructs were seeded in each well formed by the assembly of a 35 mm collagen coated coverslip with H-shaped medium size adhesive micropatterns (Cytoo, Cat#10-008-00-18) and a magnetic four-well chamber (Cytoo, Cat#30-011) following manufacturer instructions. Coverslips were fixed with 4% formaldehyde and processed for ICC as previously described (Verdier-Pinard et al., 2017). Distance measurements were performed using the Graphics line tool in Zen blue software as described in more details in Fig. 8c legend.

SDS-PAGE and Western blotting

Total protein extraction from cells in culture by scraping the cells off in NP-40 lysis buffer, separation of proteins by SDS-PAGE using NuPAGE 4-12 % gradient Bis-Tris gels (Invitrogen, Cat#NP0322BOX) and MOPS SDS running buffer (Invitrogen, Cat#NP0001-02) and Western blotting of separated proteins on nitrocellulose were performed as described previously (Verdier-Pinard et al., 2017).

Separation of septin complexes by native gel electrophoresis and detection

Native cellular protein extraction was carried out as published by Sellin et al. (Sellin et al., 2014). Briefly, proteins from cells at 80% confluence in one 100 mm petri dish were extracted in 40 μ l of native lysis buffer (80 mM PIPES pH 6.9, 2 mM $MgCl_2$, 4 mM EGTA, 0.2% saponin and protease inhibitor cocktail (Roche, Cat#04693159001); the extract was incubated

for 10 min on ice and centrifuged and the supernatant was supplemented with 0.45 M sodium chloride, incubated on ice, centrifuged, concentrated and exchanged twice with phosphate buffer (pH 7.5, 0.45 M NaCl, 1 mM EGTA and protease inhibitors) on an Amicon 30 kDa cut off concentrator (Merck, Cat# UFC 503096). Protein concentration was determined using a BCA protein assay (Thermo Scientific, Cat#23223 and 23224), glycerol was added at 1:1 (vol:vol), and extracts stored at -20°C until use. Native PAGE was performed on 4-16% NativePAGE Novex Bis-Tris polyacrylamide gels (Thermo Scientific, Cat#BN1002BOX) following instructions from the manufacturer. Briefly, native protein extracts were mixed with 4x sample buffer (Thermo Scientific, Cat#BN2003) and water (final sample buffer 1x, and about 150 mM NaCl). Eight µg of proteins were loaded per lane. Unstained native protein molecular weight standards were used (Thermo Scientific, Cat#LC0725) and stained with Coomassie blue during electrophoresis. Protein complexes were transferred overnight on a PVDF membrane under 20 V constant voltage. The membrane was partially destained with 25% MeOH and 10% acetic acid, positions of native protein molecular weight standards were marked, and the membrane was placed briefly in MeOH for complete destaining. The membrane was processed for Western blot detection following the protocol used for nitrocellulose membranes described previously (Verdier-Pinard et al., 2017).

Immunocytochemistry

Multiplex immunocytochemistry was carried out on cells cultured on collagen coated coverslips followed by 4% formaldehyde fixation as described previously (Verdier-Pinard et al., 2017). Images were acquired on a Zeiss structured light ApoTome microscope equipped with a 63x/1.4 Plan Apochromat objective and an AxioCam MRc5 camera using AxioVision software or a Zeiss LSM880 META confocal microscope equipped with a 63x/1.46 Plan Apochromat objective and a GaAsP detector using Zen software.

Co-localization of septins with microtubules and with stress fibers.

For phenotyping-analysis, individual cells were examined by ICC for co-localization of septins with total α -tubulin, acetylated K40 α -tubulin and F-actin, from top to bottom. Cells were counted as positive for co-localization of septins with microtubules or with F-actin when septin fluorescence signal was co-aligned with microtubules and/or acetylated microtubules or with ventral stress fibers, respectively. The percentage of cells positive for both septin-microtubule and septin-stress fibers co-localization, only positive for septin-stress fibers co-localization and only positive for septin-microtubule co-localization were designated in graphs as Microtubule+Actin, Actin, and Microtubule, respectively.

For assessment of SEPT9-GFP constructs co-localization with microtubules and actin fibers in individual cells, stack of images (z steps 0.85 µm) were acquired with an inverted Zeiss LSM880 META confocal microscope and a Plan Apochromat 63X /1.4NA oil objective. Co-localization analysis was achieved by image analysis with Fiji Software (Schindelin et al., 2012). Background subtraction and a Median filter were applied to each stack of GFP fluorescence images for SEPT9, Alexa fluor 647 immunofluorescence images for microtubules and Alexa fluor 350 phalloidin images for F-actin. Cytoskeletal fiber segmentation was achieved using the Directional filter and the White top hat filter of the Morphological Filter 3D in MorphoLibJ plugin (Legland et al., 2016). The obtained mask was applied to the original stack. For each staining, intensity normalization was done by dividing this stack with the Max Intensity measured through the entire stack. Before co-localization measurement, each staining was automatically threshold with the Moments method. JACoP plugin (Bolte and Cordelières, 2006) was used to calculate Manders M1 coefficients for quantitative assessment of co-localization between septin and microtubule or between septin and actin fibers in each cell.

Quantification of acetylated microtubules in cells

The fluorescence surface corresponding to acetylated microtubules in individual cells was determined using the ImageJ 1.48v software (Schneider et al., 2012): the fluorescence image of acetylated microtubules was converted in 8-bits, adjusted manually with the threshold function for black and white levels to maximally remove black pixels unrelated to acetylated microtubules, the actin image was synchronized with the acetylated microtubule image (Synchronize Windows tool) and used to delimit the ROI corresponding to the entire cell surface with the freehand selection tool, and finally the image was analysed using the measure function to obtain the percentage of surface area represented by the remaining black pixels corresponding to acetylated microtubule.

Production and purification of recombinant human septin complexes

Human septin hexameric and octameric complexes with either SEPT9_i1 or SEPT9_i3 or SEPT9_i1-i5 were produced, purified and analyzed as detailed in Iv et al (Iv et al., 2021). No difference in apparent MW was observed between recombinant septin octamers or hexamers and those extracted from cells after native gel separation and WB (Fig. S1B, C).

Septin plus microtubule reconstitution and TIRF imaging

GMPCPP-stabilized microtubule seeds serving as a nucleation site for dynamic microtubules were prepared using an established double-cycle method (Gell et al., 2010). Briefly, a ~22 μ M mixture of tubulin (~11 μ M tubulin dimers) in MRB80 (80 mM PIPES pH 6.8, 4 mM $MgCl_2$, 1 mM EGTA), composed of 75% unmodified tubulin dimers (Cytoskeleton, Inc., Ct#T240), 15% rhodamine-labeled tubulin dimers (Cytoskeleton, Inc., Cat#TL590M) and 10% biotin-modified tubulin dimers (Cytoskeleton, Inc., Cat#T333P), was spun down using an Airfuge® Air-driven ultracentrifuge (Beckman Coulter Inc., Brea, California, USA) for 5 minutes at 30 psi with a cold rotor. Then, the mixture was complemented with 1 mM GMPCPP from a 10 mM stock solution, thus diluting the tubulin to 20 μ M. This mixture was incubated at 37°C for 30 minutes to polymerize tubulin, and immediately airfuged for 5 minutes at 30 psi with the rotor at room temperature to pellet GMPCPP-stabilized microtubules. Afterwards, the supernatant was discarded and the pellet was resuspended in warm MRB80 to a final tubulin concentration of 20 μ M, considering an 80% recovery of the tubulin. The mixture was incubated on ice for 20 minutes to depolymerize the microtubules. Subsequently, it was complemented with 1 mM GMPCPP, incubated at 37°C for 30 minutes to repolymerize the microtubules, and airfuged for 5 minutes at 30 psi with a warm rotor. The pellet, containing GMPCPP-stabilized microtubule seeds, was resuspended in warm MRB80 supplemented with 10% glycerol, snap-frozen, and kept at -80°C until use.

Nr. 1 Menzel coverslips (Thermo Fisher scientific, product number 11961988) and glass slides (Thermo Fisher scientific, product number 11879022) were cleaned in base piranha solution (5% hydrogen peroxide, 5% ammonium hydroxide) at 70°C for 10 minutes, washed extensively by rinsing with Milli-Q water and stored in Milli-Q water for up to 5 days. Just before use, a coverslip and a glass slide were blow dried with a stream of N_2 gas. Flow channels were prepared by placing parallel 2x20 mm parafilm strips spaced by 2-3 mm between the glass slide and the coverslip. The parafilm was melted by placing the chambers on a hotplate at 120°C. After cooling down, the chambers were passivated by incubation with 0.2 mg/mL Poly(L-lysine)-graft-biotinylated PEG (SuSoS, product number CHF560.00) in MRB80, 0.2 mg/mL neutravidin in MRB80, 0.5mg/mL κ -casein in MRB80, and 1 wt% Pluronic F-127 in MRB80, in that order and without intervening washing steps. The channels were washed with three channel volumes (~30 μ L) of MRB80 at the end of the passivation process. Then the channels were incubated for 10 minutes with an aliquot of GMPCPP-stabilized seeds that was quickly thawed at 37°C, allowing the microtubule seeds to bind to

the surface via biotin-neutravidin interactions. Microtubule polymerization was induced by immediately flushing into the channel 20 μ M tubulin (3% rhodamine-labeled tubulin) in a 5:1 volume ratio of MRB80:septin buffer complemented with 0.5 mg/mL κ -casein to prevent unspecific interactions, 0.1% methylcellulose as a crowding agent, 1 mM ATP, 1 mM GTP and an oxygen scavenging system composed of 50 mM glucose, 200 μ g/ml catalase, 400 μ g/ml glucose-oxidase, and 4 mM DTT. A mixture of 90% unlabelled and 10% msGFP-labeled septin hetero-hexamers or hetero-octamers (containing either SEPT9_i1 or SEPT9_i3) were added to the previous mix at different concentrations in the range of 10 to 300 nM.

The samples were immediately imaged using a Nikon Ti2-E microscope complemented with a Gataca iLAS2 azimuthal TIRF illumination system heated to 30°C using an Okolab incubator system. The sample was illuminated with 488-nm and 561-nm lasers (Gataca laser combiner iLAS2) to visualize the septin and the tubulin signals, respectively. To achieve fast imaging, the fluorescence signal was split with a Cairn Research Optosplit II ByPass containing a Chroma ZT 543 rdc dichroic mirror and filtered with either a 525/50 or a 600/50 chroma bandpass filter. The images were recorded with a Andor iXon Ultra 897 EM-CCD camera using an exposure time of 75 ms, for 10-20 minutes with a frame rate of 1 frame/second.

Microtubule dynamics were analysed by kymograph analysis (Bieling et al., 2007). Kymographs were built with the reslice tool in FIJI (Schneider et al., 2012) on a manually drawn line that went from the beginning of the microtubule seed to the tip of the microtubule in its maximum length. In the kymographs, we can observe the positions of the microtubule tips over time. The analysis was only done on the plus ends of the microtubules, which can be distinguished from the minus ends via the longer final length and higher growth velocity of the former. Growth and shortening rates were obtained as the slopes of manually fitted straight lines on the growing or shortening contour phases, determined by manual inspection, of the microtubule plus ends. The catastrophe rate was calculated as the inverse of the time that a microtubule spends growing.

Statistical analysis

Unless indicated otherwise, statistical analysis was performed using GraphPad Prism software and unpaired two-tailed t-test with Welch correction for cell related data or using the function `compare_means` from the package `ggpubr` from R and two-tailed t-test with Benjamini & Hochberg p-value correction (<https://rpkgs.datanovia.com/ggpubr/index.html>) for the *in vitro* data related to microtubule dynamics.

Acknowledgements

We thank Jeffrey den Haan (TU Delft, The Netherlands) for help with protein purification.

Competing interests

The authors declare no competing or financial interests

Author contributions

Conceptualization: G.H.K., A.B., M.M., P.V.-P.; Methodology: M.M., P.V.-P.; Investigation: M.K., G.C.L., J. L. F., F.I., D.S., A. L., M.G., M. B., Y. L., K.A., M. R., D. I., M.M., P.V.-P.; Resources: T.T.; Writing original draft: P.V.-P.; Writing-review & editing: M.K., G.C.L.

M.R., D. I., G.H.K., A. B., M.M., P.V.-P.; Supervision: T.T., A. B., G. H. K., M.M., P.V.-P.; Project administration: P.V.-P., Funding acquisition: T.T., A.B., G.H.K., M.M., P.V.-P.

Funding

This research received funding from the Agence Nationale de la Recherche (ANR grant ANR-17-CE13-0014; SEPTIMORF) (to M.M. and P. V-P.) and the Nederlandse Organisatie voor Wetenschappelijk Onderzoek (NWO/OCW) through the ‘BaSyC-Building a Synthetic Cell’ Gravitation grant (024.003.019) (to G.K.).

References

- Addi, C., Bai, J. and Echard, A. (2018). Actin, microtubule, septin and ESCRT filament remodeling during late steps of cytokinesis. *Curr Opin Cell Biol* **50**, 27-34.
- Bai, X., Bowen, J. R., Knox, T. K., Zhou, K., Pendziwiat, M., Kuhlenbaumer, G., Sindelar, C. V. and Spiliotis, E. T. (2013). Novel septin 9 repeat motifs altered in neuralgic amyotrophy bind and bundle microtubules. *J Cell Biol* **203**, 895-905.
- Bertin, A., McMurray, M. A., Pierson, J., Thai, L., McDonald, K. L., Zehr, E. A., Garcia, G., 3rd, Peters, P., Thorner, J. and Nogales, E. (2012). Three-dimensional ultrastructure of the septin filament network in *Saccharomyces cerevisiae*. *Mol Biol Cell* **23**, 423-32.
- Bertin, A., McMurray, M. A., Thai, L., Garcia, G., 3rd, Votin, V., Grob, P., Allyn, T., Thorner, J. and Nogales, E. (2010). Phosphatidylinositol-4,5-bisphosphate promotes budding yeast septin filament assembly and organization. *J Mol Biol* **404**, 711-31.
- Bieling, P., Laan, L., Schek, H., Munteanu, E. L., Sandblad, L., Dogterom, M., Brunner, D. and Surrey, T. (2007). Reconstitution of a microtubule plus-end tracking system in vitro. *Nature* **450**, 1100-5.
- Boite, S. and Cordelieres, F. P. (2006). A guided tour into subcellular colocalization analysis in light microscopy. *J Microsc* **224**, 213-32.
- Bowen, J. R., Hwang, D., Bai, X., Roy, D. and Spiliotis, E. T. (2011). Septin GTPases spatially guide microtubule organization and plus end dynamics in polarizing epithelia. *J Cell Biol* **194**, 187-97.
- Buschmann, H., Chan, J., Sanchez-Pulido, L., Andrade-Navarro, M. A., Doonan, J. H. and Lloyd, C. W. (2006). Microtubule-associated AIR9 recognizes the cortical division site at preprophase and cell-plate insertion. *Curr Biol* **16**, 1938-43.
- Calvo, F., Ranftl, R., Hooper, S., Farrugia, A. J., Moeendarbary, E., Bruckbauer, A., Batista, F., Charras, G. and Sahai, E. (2015). Cdc42EP3/BORG2 and Septin Network Enables Mechano-transduction and the Emergence of Cancer-Associated Fibroblasts. *Cell Rep* **13**, 2699-714.
- Carlton, J. G., Jones, H. and Eggert, U. S. (2020). Membrane and organelle dynamics during cell division. *Nat Rev Mol Cell Biol* **21**, 151-166.
- Chang, W., Gruber, D., Chari, S., Kitazawa, H., Hamazumi, Y., Hisanaga, S. and Bulinski, J. C. (2001). Phosphorylation of MAP4 affects microtubule properties and cell cycle progression. *J Cell Sci* **114**, 2879-87.
- Collie, A. M., Landsverk, M. L., Ruzzo, E., Mefford, H. C., Buysse, K., Adkins, J. R., Knutzen, D. M., Barnett, K., Brown, R. H., Jr., Parry, G. J. et al. (2010). Non-recurrent SEPT9 duplications cause hereditary neuralgic amyotrophy. *J Med Genet* **47**, 601-7.
- Connolly, D., Abdesselam, I., Verdier-Pinard, P. and Montagna, C. (2011a). Septin roles in tumorigenesis. *Biol Chem* **392**, 725-38.

Connolly, D., Yang, Z., Castaldi, M., Simmons, N., Oktay, M. H., Coniglio, S., Fazzari, M. J., Verdier-Pinard, P. and Montagna, C. (2011b). Septin 9 isoform expression, localization and epigenetic changes during human and mouse breast cancer progression. *Breast Cancer Res* **13**, R76.

Costantini, L. M., Fossati, M., Francolini, M. and Snapp, E. L. (2012). Assessing the tendency of fluorescent proteins to oligomerize under physiologic conditions. *Traffic* **13**, 643-9.

Cranfill, P. J., Sell, B. R., Baird, M. A., Allen, J. R., Lavagnino, Z., de Gruiter, H. M., Kremers, G. J., Davidson, M. W., Ustione, A. and Piston, D. W. (2016). Quantitative assessment of fluorescent proteins. *Nat Methods* **13**, 557-62.

DeRose, B. T., Kelley, R. S., Ravi, R., Kokona, B., Beld, J., Spiliotis, E. T. and Padrick, S. B. (2020). Production and analysis of a mammalian septin hetero-octamer complex. *Cytoskeleton (Hoboken)* **77**, 485-499.

Dogterom, M. and Koenderink, G. H. (2019). Actin-microtubule crosstalk in cell biology. *Nat Rev Mol Cell Biol* **20**, 38-54.

Estey, M. P., Di Ciano-Oliveira, C., Froese, C. D., Bejide, M. T. and Trimble, W. S. (2010). Distinct roles of septins in cytokinesis: SEPT9 mediates midbody abscission. *J Cell Biol* **191**, 741-9.

Estey, M. P., Di Ciano-Oliveira, C., Froese, C. D., Fung, K. Y. Y., Steels, J. D., Litchfield, D. W. and Trimble, W. S. (2013). Mitotic regulation of SEPT9 protein by cyclin-dependent kinase 1 (Cdk1) and Pin1 protein is important for the completion of cytokinesis. *J Biol Chem* **288**, 30075-30086.

Farrugia, A. J., Rodriguez, J., Orgaz, J. L., Lucas, M., Sanz-Moreno, V. and Calvo, F. (2020). CDC42EP5/BORG3 modulates SEPT9 to promote actomyosin function, migration, and invasion. *J Cell Biol* **219**.

Froidevaux-Klipfel, L., Targa, B., Cantaloube, I., Ahmed-Zaid, H., Pous, C. and Baillet, A. (2015). Septin cooperation with tubulin polyglutamylation contributes to cancer cell adaptation to taxanes. *Oncotarget* **6**, 36063-80.

Fung, K. Y., Dai, L. and Trimble, W. S. (2014). Cell and molecular biology of septins. *Int Rev Cell Mol Biol* **310**, 289-339.

Gell, C., Bormuth, V., Brouhard, G. J., Cohen, D. N., Diez, S., Friel, C. T., Helenius, J., Nitzsche, B., Petzold, H., Ribbe, J. et al. (2010). Microtubule dynamics reconstituted in vitro and imaged by single-molecule fluorescence microscopy. *Methods Cell Biol* **95**, 221-45.

Ghossoub, R., Hu, Q., Failler, M., Rouyez, M. C., Spitzbarth, B., Mostowy, S., Wolfrum, U., Saunier, S., Cossart, P., Jamesnelson, W. et al. (2013). Septins 2, 7 and 9 and MAP4 colocalize along the axoneme in the primary cilium and control ciliary length. *J Cell Sci* **126**, 2583-94.

Hannibal, M. C., Ruzzo, E. K., Miller, L. R., Betz, B., Buchan, J. G., Knutzen, D. M., Barnett, K., Landsverk, M. L., Brice, A., LeGuern, E. et al. (2009). SEPT9 gene sequencing analysis reveals recurrent mutations in hereditary neuralgic amyotrophy. *Neurology* **72**, 1755-9.

Hein, M. Y., Hubner, N. C., Poser, I., Cox, J., Nagaraj, N., Toyoda, Y., Gak, I. A., Weisswange, I., Mansfeld, J., Buchholz, F. et al. (2015). A human interactome in three quantitative dimensions organized by stoichiometries and abundances. *Cell* **163**, 712-23.

Hu, J., Bai, X., Bowen, J. R., Dolat, L., Korobova, F., Yu, W., Baas, P. W., Svitekina, T., Gallo, G. and Spiliotis, E. T. (2012). Septin-driven coordination of actin and microtubule remodeling regulates the collateral branching of axons. *Curr Biol* **22**, 1109-15.

Iv, F., Martins, C. S., Castro-Linares, G., Taveneau, C., Barbier, P., Verdier-Pinard, P., Camoin, L., Audebert, S., Tsai, F.-C., Ramond, L. et al. (2021). Insights into animal septins using recombinant human septin octamers with distinct SEPT9 isoforms. *J Cell Sci* **134**, jcs258484.

Janke, C. and Magiera, M. M. (2020). The tubulin code and its role in controlling microtubule properties and functions. *Nat Rev Mol Cell Biol* **21**, 307-326.

Janke, C. and Montagnac, G. (2017). Causes and Consequences of Microtubule Acetylation. *Curr Biol* **27**, R1287-R1292.

Karasmanis, E. P., Phan, C. T., Angelis, D., Kesisova, I. A., Hoogenraad, C. C., McKenney, R. J. and Spiliotis, E. T. (2018). Polarity of Neuronal Membrane Traffic Requires Sorting of Kinesin Motor Cargo during Entry into Dendrites by a Microtubule-Associated Septin. *Dev Cell* **46**, 518-524.

Kellogg, E. H., Hejab, N. M. A., Poepsel, S., Downing, K. H., DiMaio, F. and Nogales, E. (2018). Near-atomic model of microtubule-tau interactions. *Science* **360**, 1242-1246.

Kim, M. S., Froese, C. D., Estey, M. P. and Trimble, W. S. (2011). SEPT9 occupies the terminal positions in septin octamers and mediates polymerization-dependent functions in abscission. *J Cell Biol* **195**, 815-26.

Kim, M. S., Froese, C. D., Xie, H. and Trimble, W. S. (2012). Uncovering principles that control septin-septin interactions. *J Biol Chem* **287**, 30406-13.

Kinoshita, M., Field, C. M., Coughlin, M. L., Straight, A. F. and Mitchison, T. J. (2002). Self- and actin-templated assembly of Mammalian septins. *Dev Cell* **3**, 791-802.

Kinoshita, M., Kumar, S., Mizoguchi, A., Ide, C., Kinoshita, A., Haraguchi, T., Hiraoka, Y. and Noda, M. (1997). Nedd5, a mammalian septin, is a novel cytoskeletal component interacting with actin-based structures. *Genes Dev* **11**, 1535-47.

Kuhlenbaumer, G., Hannibal, M. C., Nelis, E., Schirmacher, A., Verpoorten, N., Meuleman, J., Watts, G. D., De Vriendt, E., Young, P., Stogbauer, F. et al. (2005). Mutations in SEPT9 cause hereditary neuralgic amyotrophy. *Nat Genet* **37**, 1044-6.

Legland, D., Arganda-Carreras, I. and Andrey, P. (2016). MorphoLibJ: integrated library and plugins for mathematical morphology with ImageJ. *Bioinformatics* **32**, 3532-3534.

Maninova, M., Caslavsky, J. and Vomastek, T. (2017). The assembly and function of perinuclear actin cap in migrating cells. *Protoplasma* **254**, 1207-1218.

Marquardt, J., Chen, X. and Bi, E. (2019). Architecture, remodeling, and functions of the septin cytoskeleton. *Cytoskeleton (Hoboken)* **76**, 7-14.

McIlhatton, M. A., Burrows, J. F., Donaghy, P. G., Chanduloy, S., Johnston, P. G. and Russell, S. E. (2001). Genomic organization, complex splicing pattern and expression of a human septin gene on chromosome 17q25.3. *Oncogene* **20**, 5930-9.

Mendonca, D. C., Macedo, J. N., Guimaraes, S. L., Barroso da Silva, F. L., Cassago, A., Garratt, R. C., Portugal, R. V. and Araujo, A. P. U. (2019). A revised order of subunits in mammalian septin complexes. *Cytoskeleton (Hoboken)* **76**, 457-466.

Mostowy, S. and Cossart, P. (2012). Septins: the fourth component of the cytoskeleton. *Nat Rev Mol Cell Biol* **13**, 183-94.

Nagata, K., Kawajiri, A., Matsui, S., Takagishi, M., Shiromizu, T., Saitoh, N., Izawa, I., Kiyono, T., Itoh, T. J., Hotani, H. et al. (2003). Filament formation of MSF-A, a mammalian septin, in human mammary epithelial cells depends on interactions with microtubules. *J Biol Chem* **278**, 18538-43.

Nakos, K., Radler, M. R. and Spiliotis, E. T. (2019a). Septin 2/6/7 complexes tune microtubule plus-end growth and EB1 binding in a concentration- and filament-dependent manner. *Mol Biol Cell* **30**, 2913-2928.

- Nakos, K., Rosenberg, M. and Spiliotis, E. T.** (2019b). Regulation of microtubule plus end dynamics by septin 9. *Cytoskeleton (Hoboken)* **76**, 83-91.
- Nolke, T., Schwan, C., Lehmann, F., Ostevold, K., Pertz, O. and Aktories, K.** (2016). Septins guide microtubule protrusions induced by actin-depolymerizing toxins like *Clostridium difficile* transferase (CDT). *Proc Natl Acad Sci U S A* **113**, 7870-5.
- Oegema, K., Savoian, M. S., Mitchison, T. J. and Field, C. M.** (2000). Functional analysis of a human homologue of the *Drosophila* actin binding protein anillin suggests a role in cytokinesis. *J Cell Biol* **150**, 539-52.
- Ong, K., Wloka, C., Okada, S., Svitkina, T. and Bi, E.** (2014). Architecture and dynamic remodelling of the septin cytoskeleton during the cell cycle. *Nat Commun* **5**, 5698.
- Ostevold, K., Melendez, A. V., Lehmann, F., Schmidt, G., Aktories, K. and Schwan, C.** (2017). Septin remodeling is essential for the formation of cell membrane protrusions (microtentacles) in detached tumor cells. *Oncotarget* **8**, 76686-76698.
- Pedelacq, J. D., Cabantous, S., Tran, T., Terwilliger, T. C. and Waldo, G. S.** (2006). Engineering and characterization of a superfolder green fluorescent protein. *Nat Biotechnol* **24**, 79-88.
- Renshaw, M. J., Liu, J., Lavoie, B. D. and Wilde, A.** (2014). Anillin-dependent organization of septin filaments promotes intercellular bridge elongation and Chmp4B targeting to the abscission site. *Open Biol* **4**, 130190.
- Schindelin, J., Arganda-Carreras, I., Frise, E., Kaynig, V., Longair, M., Pietzsch, T., Preibisch, S., Rueden, C., Saalfeld, S., Schmid, B. et al.** (2012). Fiji: an open-source platform for biological-image analysis. *Nat Methods* **9**, 676-82.
- Schneider, C. A., Rasband, W. S. and Eliceiri, K. W.** (2012). NIH Image to ImageJ: 25 years of image analysis. *Nat Methods* **9**, 671-5.
- Sellin, M. E., Stenmark, S. and Gullberg, M.** (2012). Mammalian SEPT9 isoforms direct microtubule-dependent arrangements of septin core heteromers. *Mol Biol Cell* **23**, 4242-55.
- Sellin, M. E., Stenmark, S. and Gullberg, M.** (2014). Cell type-specific expression of SEPT3-homology subgroup members controls the subunit number of heteromeric septin complexes. *Mol Biol Cell* **25**, 1594-607.
- Serrano, L., Montejo de Garcini, E., Hernandez, M. A. and Avila, J.** (1985). Localization of the tubulin binding site for tau protein. *Eur J Biochem* **153**, 595-600.
- Shaner, N. C., Lin, M. Z., McKeown, M. R., Steinbach, P. A., Hazelwood, K. L., Davidson, M. W. and Tsien, R. Y.** (2008). Improving the photostability of bright monomeric orange and red fluorescent proteins. *Nat Methods* **5**, 545-51.
- Shida, T., Cueva, J. G., Xu, Z., Goodman, M. B. and Nachury, M. V.** (2010). The major alpha-tubulin K40 acetyltransferase alphaTAT1 promotes rapid ciliogenesis and efficient mechanosensation. *Proc Natl Acad Sci U S A* **107**, 21517-22.
- Shigematsu, H., Imasaki, T., Doki, C., Sumi, T., Aoki, M., Uchikubo-Kamo, T., Sakamoto, A., Tokuraku, K., Shirouzu, M. and Nitta, R.** (2018). Structural insight into microtubule stabilization and kinesin inhibition by Tau family MAPs. *J Cell Biol* **217**, 4155-4163.
- Sirajuddin, M., Farkasovsky, M., Hauer, F., Kuhlmann, D., Macara, I. G., Weyand, M., Stark, H. and Wittinghofer, A.** (2007). Structural insight into filament formation by mammalian septins. *Nature* **449**, 311-5.
- Sneider, A., Hah, J., Wirtz, D. and Kim, D. H.** (2019). Recapitulation of molecular regulators of nuclear motion during cell migration. *Cell Adh Migr* **13**, 50-62.

Soroor, F., Kim, M. S., Palander, O., Balachandran, Y., Collins, R. F., Benlekbir, S., Rubinstein, J. L. and Trimble, W. S. (2021). Revised subunit order of mammalian septin complexes explains their in vitro polymerization properties. *Mol Biol Cell* **32**, 289-300.

Spiliotis, E. T. (2010). Regulation of microtubule organization and functions by septin GTPases. *Cytoskeleton (Hoboken)* **67**, 339-45.

Spiliotis, E. T., Hunt, S. J., Hu, Q., Kinoshita, M. and Nelson, W. J. (2008). Epithelial polarity requires septin coupling of vesicle transport to polyglutamylated microtubules. *J Cell Biol* **180**, 295-303.

Straight, A. F. and Field, C. M. (2000). Microtubules, membranes and cytokinesis. *Curr Biol* **10**, R760-70.

Surka, M. C., Tsang, C. W. and Trimble, W. S. (2002). The mammalian septin MSF localizes with microtubules and is required for completion of cytokinesis. *Mol Biol Cell* **13**, 3532-45.

Szuba, A., Bano, F., Iv, F., Mavrakis, M., Richter, R. P., Bertin, A. and Koenderink, G. H. (2020). Membrane binding controls ordered self-assembly of animal septins. *bioRxiv*, 2020.09.22.307918.

Tada, T., Simonetta, A., Batterton, M., Kinoshita, M., Edbauer, D. and Sheng, M. (2007). Role of Septin cytoskeleton in spine morphogenesis and dendrite development in neurons. *Curr Biol* **17**, 1752-8.

Targa, B., Klipfel, L., Cantaloube, I., Salameh, J., Benoit, B., Pous, C. and Baillet, A. (2019). Septin filament coalignment with microtubules depends on SEPT9_i1 and tubulin polyglutamylation, and is an early feature of acquired cell resistance to paclitaxel. *Cell Death Dis* **10**, 54.

Thery, M., Pepin, A., Dressaire, E., Chen, Y. and Bornens, M. (2006). Cell distribution of stress fibres in response to the geometry of the adhesive environment. *Cell Motil Cytoskeleton* **63**, 341-55.

Valadares, N. F., d' Muniz Pereira, H., Ulian Araujo, A. P. and Garratt, R. C. (2017). Septin structure and filament assembly. *Biophys Rev* **9**, 481-500.

Verdier-Pinard, P., Salaun, D., Bouguenina, H., Shimada, S., Pophillat, M., Audebert, S., Agavonian, E., Coslet, S., Charafe-Jauffret, E., Tachibana, T. et al. (2017). Septin 9_i2 is downregulated in tumors, impairs cancer cell migration and alters subnuclear actin filaments. *Sci Rep* **7**, 44976.

Verma, V. and Maresca, T. J. (2019). Microtubule plus-ends act as physical signaling hubs to activate RhoA during cytokinesis. *Elife* **8**.

Wang, S., Li, W., Liu, S. and Xu, J. (2016). RaptorX-Property: a web server for protein structure property prediction. *Nucleic Acids Res* **44**, W430-5.

Woods, B. L. and Gladfelter, A. S. (2020). The state of the septin cytoskeleton from assembly to function. *Curr Opin Cell Biol* **68**, 105-112.

Xu, J., McPartlon, M. and Li, J. (2021). Improved protein structure prediction by deep learning irrespective of co-evolution information. *Nat Mach Intell* **3**, 601-609.

Yadav, S., Osés-Prieto, J. A., Peters, C. J., Zhou, J., Pleasure, S. J., Burlingame, A. L., Jan, L. Y. and Jan, Y. N. (2017). TAOK2 Kinase Mediates PSD95 Stability and Dendritic Spine Maturation through Septin7 Phosphorylation. *Neuron* **93**, 379-393.

Zacharias, D. A., Violin, J. D., Newton, A. C. and Tsien, R. Y. (2002). Partitioning of lipid-modified monomeric GFPs into membrane microdomains of live cells. *Science* **296**, 913-6.

Figures

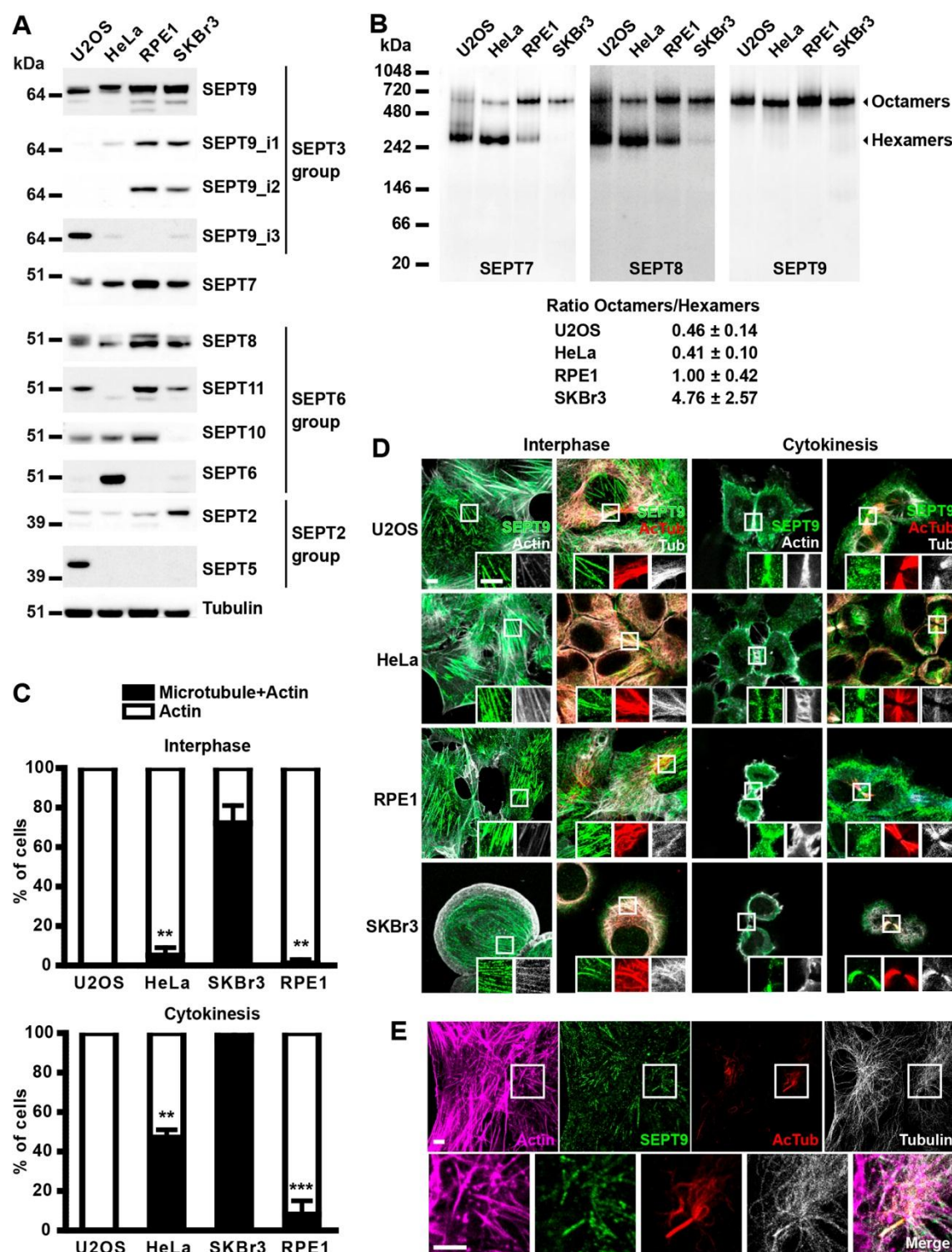


Fig. 1. SEPT9 expression, incorporation in octamers and localization in human cell lines. (A) Western blots of total protein extracts from U2OS, HeLa, RPE1 and SKBr3 cells probed with antibodies against septins and tubulin. (B) Native extracts from the same cell lines were analyzed by Western blotting for their content in both septin hexamers and octamers using antibodies against constitutively required SEPT7 and ubiquitously expressed SEPT8; septin

octamers were also specifically labeled with a pan SEPT9 antibody. Relative content in septin octamers and hexamers in each cell line based on three independent SEPT7 WB is presented below the blots (mean \pm SEM). (C, D) Cellular localization by immunocytochemistry of SEPT9, α -tubulin (Tub), acetylated tubulin (AcTub) and actin in the same cell lines, during interphase and cytokinesis; in (C), the percentage of cells displaying both co-localization of SEPT9 with microtubules and co-localization with stress fibers (Microtubule + Actin) or only stress fibers (Actin) was determined from three independent experiments based on a total of 90 cells (30 cells per experiment). Unpaired, two-tailed t-test with Welch's correction, ** $p < 0.01$, *** $p < 0.0005$, Microtubule + Actin localization relative to SKBr3 cells; in (D), scale bars correspond to 5 μ m, insets are two-fold zoomed regions framed by a white square in the corresponding original images. (E) RPE1 cells were starved for 24 h and immunofluorescence was performed as in (D); scale bars correspond to 5 μ m, a three-fold zoom of a region framed in white containing a primary cilium is presented below the original images.

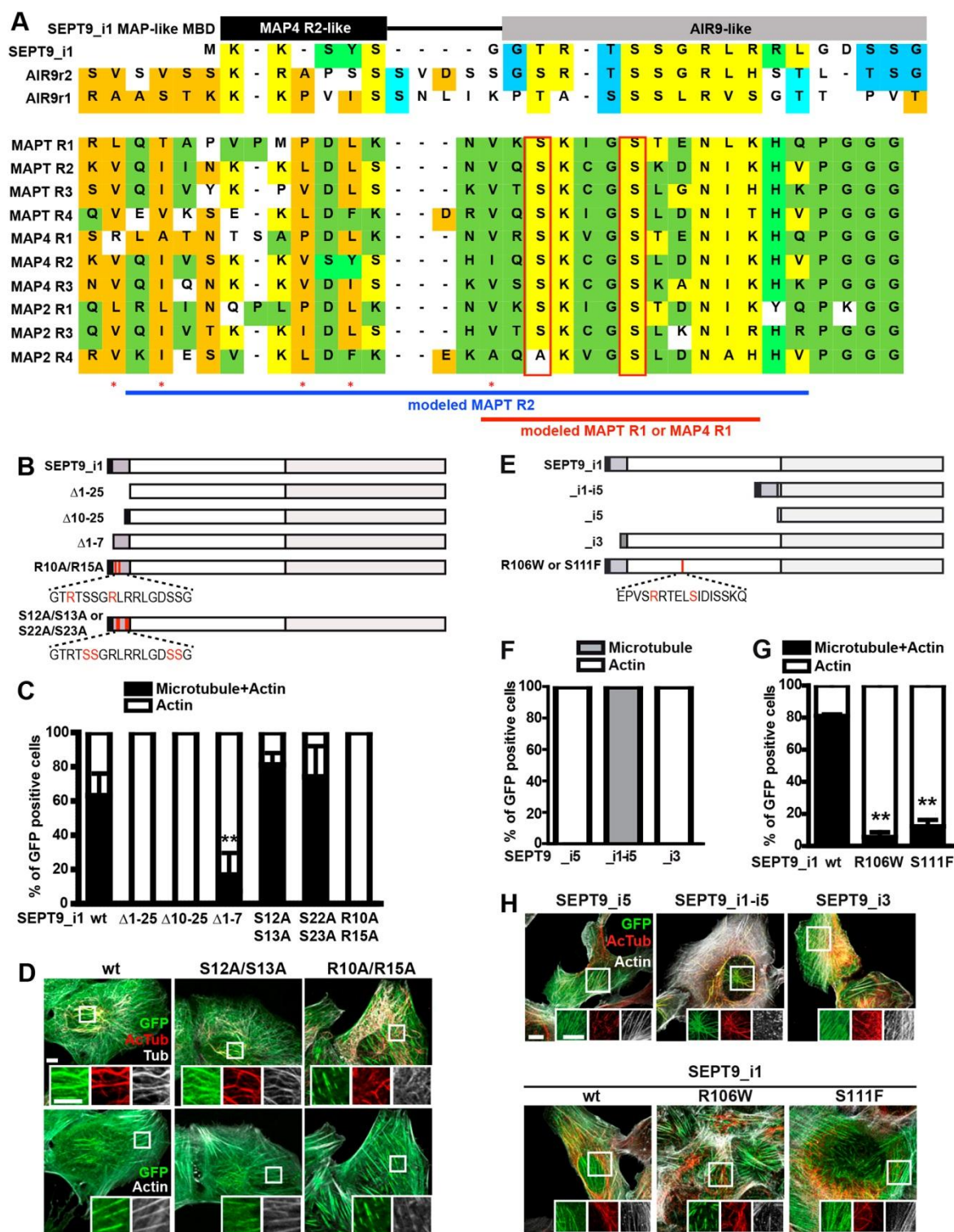


Fig. 2. Identification of the microtubule-binding domain in SEPT9_i1. (A) Top part: human SEPT9_i1 specific amino-acid N-terminal sequence (1-24) was aligned with the homologous plant *A. thaliana* AIR9 sequences (173-205 and 46-78) contained in the AIR-9 microtubule binding domain (MBD) (Bushman et al. 2006); bottom part: SEPT9_i1 and AIR9 sequences in top part were aligned with sequences of tandem repeats involved in the binding of human structural MAPs (MAPT, MAP4 and MAP2) to microtubules (ex: MAPT 4R isoform positions of repeats are R1₂₄₂₋₂₇₃, R2₂₇₄₋₃₀₄, R3₃₀₅₋₃₃₅ and R4₃₃₆₋₃₆₇). Alignments were adjusted by introducing gaps and similar amino acid residues were manually coded,

orange: common to AIR9 and MAPs; yellow: common to SEPT9_i1, AIR9 and MAPs; light green: common to SEPT9_i1 and MAPs; dark green: common to MAPs; dark blue: common to SEPT9_i1 and AIR9; light blue: common to AIR9 repeats. Important serine residues and hydrophobic residues of MAPs involved in MAP repeat-microtubule lattice interactions are framed in red and marked with a red asterisk, respectively. Horizontal blue line and red line indicate, respectively, the position of MAPT R2 repeat and MAPT R1/MAP4 R1 repeat modeled from the cryo-EM structural determination of MAP repeated sequences bound on microtubules *in vitro* (Kellogg et al., 2018, Shigematsu et al., 2018). (B) Schematic representation of the SEPT9_i1 constructs mutated in the predicted MBD. Filling color code: black, MAP4 R2-like sequence; dark grey, AIR9-like sequence; white, N-terminus common to long isoforms; light grey, G-domain. (C, D) Co-localization of each SEPT9 construct tagged with GFP at the C-terminus transfected in U2OS cells with microtubules or stress fibers during interphase was analyzed as described in Fig. 1. Unpaired, two-tailed t-test with Welch's correction, ** $p < 0.01$, Microtubule + Actin localization relative to SEPT9_i1 wt. (D) Representative images are shown; scale bars: 5 μm ; insets: three-fold zooms. (E) Schematic representation of SEPT9 isoforms (SEPT9_i1, _i5 and _i3), chimeric construct fusing SEPT9_i1 MBD to the N-terminus of SEPT9_i5 (SEPT9_i1-i5) and SEPT9_i1 HNA mutants. Filling color code same as in (B). (F-H) Co-localization of SEPT9_i5, _i1-i5 or _i3, (F) and of SEPT9 HNA point mutants (G) tagged with GFP at the C-terminus with microtubules or stress fibers transfected in interphase U2OS cells, was quantified as in Fig. 1. Unpaired, two-tailed t-test with Welch's correction, ** $p < 0.01$. (H) Representative images are shown; scale bars 10 μm , insets: 1.4-fold zooms.

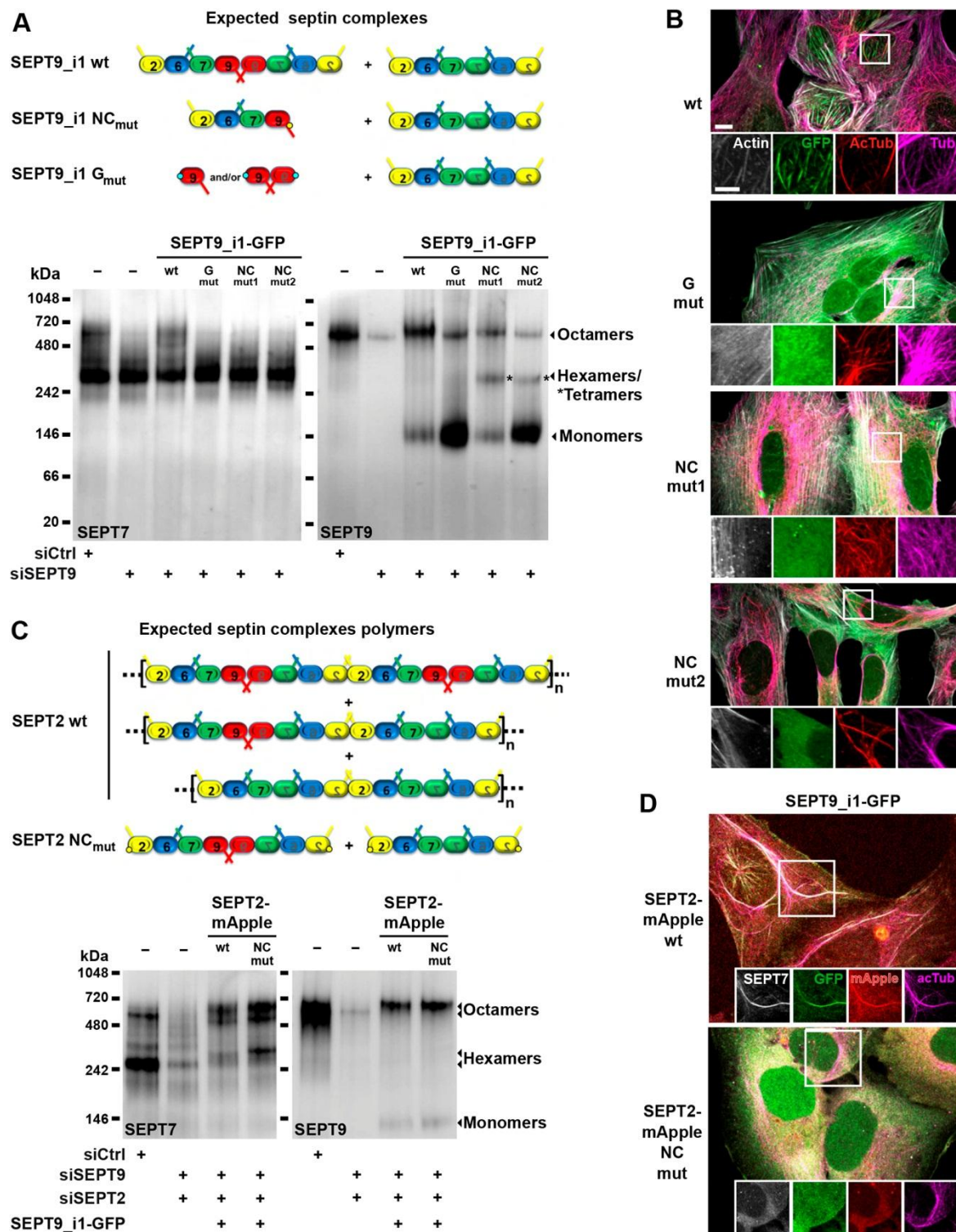


Fig. 3. Dependence of septin association with microtubules on the incorporation of SEPT9_i1 in polymerized septin octamers. (A) Top, predicted septin complexes when SEPT9_i1 wt or SEPT9_i1 mutated on its G (G_{mut}, blue dots) or NC interface (NC_{mut}, yellow dot) is expressed in cells; bottom, Western blots of native gels resolving septin complexes present in U2OS cells transfected with indicated siRNA (Ctrl=Control) and expressing SEPT9_i1 wt or SEPT9_i1 interface mutants. (B) GFP-fluorescence based co-localization of SEPT9_i1 wt or interface mutants with actin, acetylated microtubules (AcTub) and microtubules (Tub); SEPT9_i1 wt co-localized with both microtubules and actin fibers as

expected, but non-octameric septin complexes containing an interface mutant SEPT9_i1 did not. Scale bar 10 μm , insets: two-fold zooms of framed regions. (C) Top, predicted septin complexes when SEPT2 wt or SEPT2 mutated on its NC interface (NC_{mut}, yellow dots) is co-expressed with SEPT9_i1 in U2OS cells; bottom, Western blots of native gels resolving septin complexes present in U2OS expressing indicated siRNAs and septin constructs. (D) mApple and GFP-based co-localization of SEPT2 and SEPT9_i1, respectively, with actin and acetylated microtubules; expression of SEPT2 NC mutant prevented normal co-localization of octamers harboring SEPT9_i1 with acetylated microtubules and actin fibers. Insets: individual fluorescence channel images of framed regions.

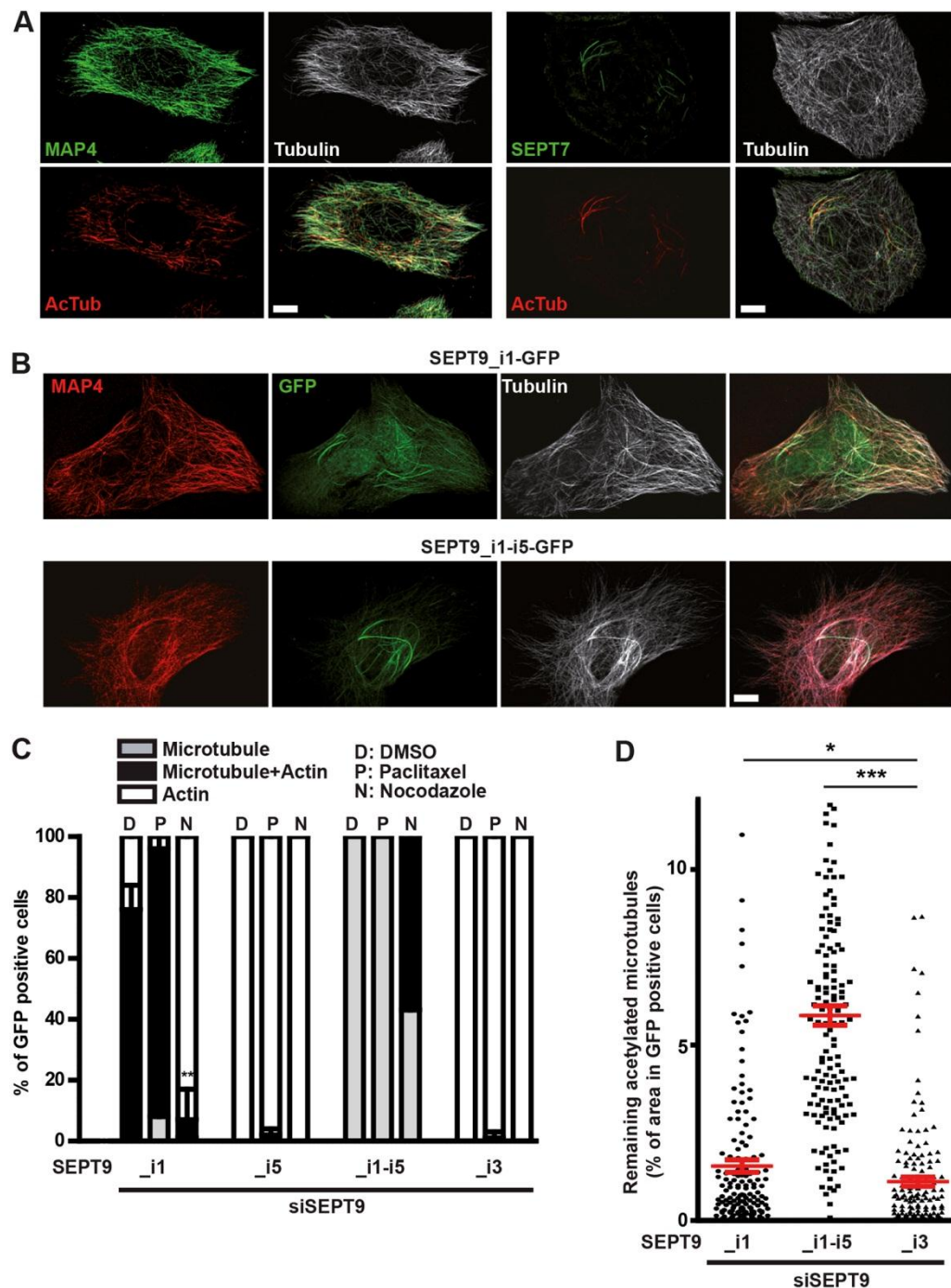


Fig. 4. SEPT9_i1 selective binding on, and stabilization of, microtubule bundles. (A) Differential co-localization of endogenous SEPT7 vs MAP4 with microtubule cytoskeleton in SKBr3 cells. (B) Differential co-localization between endogenous MAP4 and transfected SEPT9_i1-GFP or SEPT9_i1-i5-GFP with microtubule cytoskeleton in U2OS cells. Scale bars, 5 μ m. (C) The percentage of U2OS cells, knocked down for SEPT9 and expressing the indicated SEPT9-GFP constructs, displaying microtubule, actin or mixed co-localization with GFP, was evaluated upon treatment with DMSO vehicle, 2 μ M paclitaxel or 10 μ M nocodazole for 2 hrs. Results are from a total of 90 cells from three independent experiments based (30 cells per experiment). Unpaired, two-tailed t-test with Welch's correction, ** $p < 0.01$, * $p < 0.05$, *** $p < 0.001$.

0.01, Microtubule + Actin localization relative to DMSO. (D) Quantification of nocodazole-resistant acetylated microtubules in U2OS treated as in (C). Results are from a total of 150 cells from three independent experiments (50 cells per experiments). Unpaired, two-tailed t-test with Welch's correction, * $p < 0.05$, *** $p < 0.0005$.

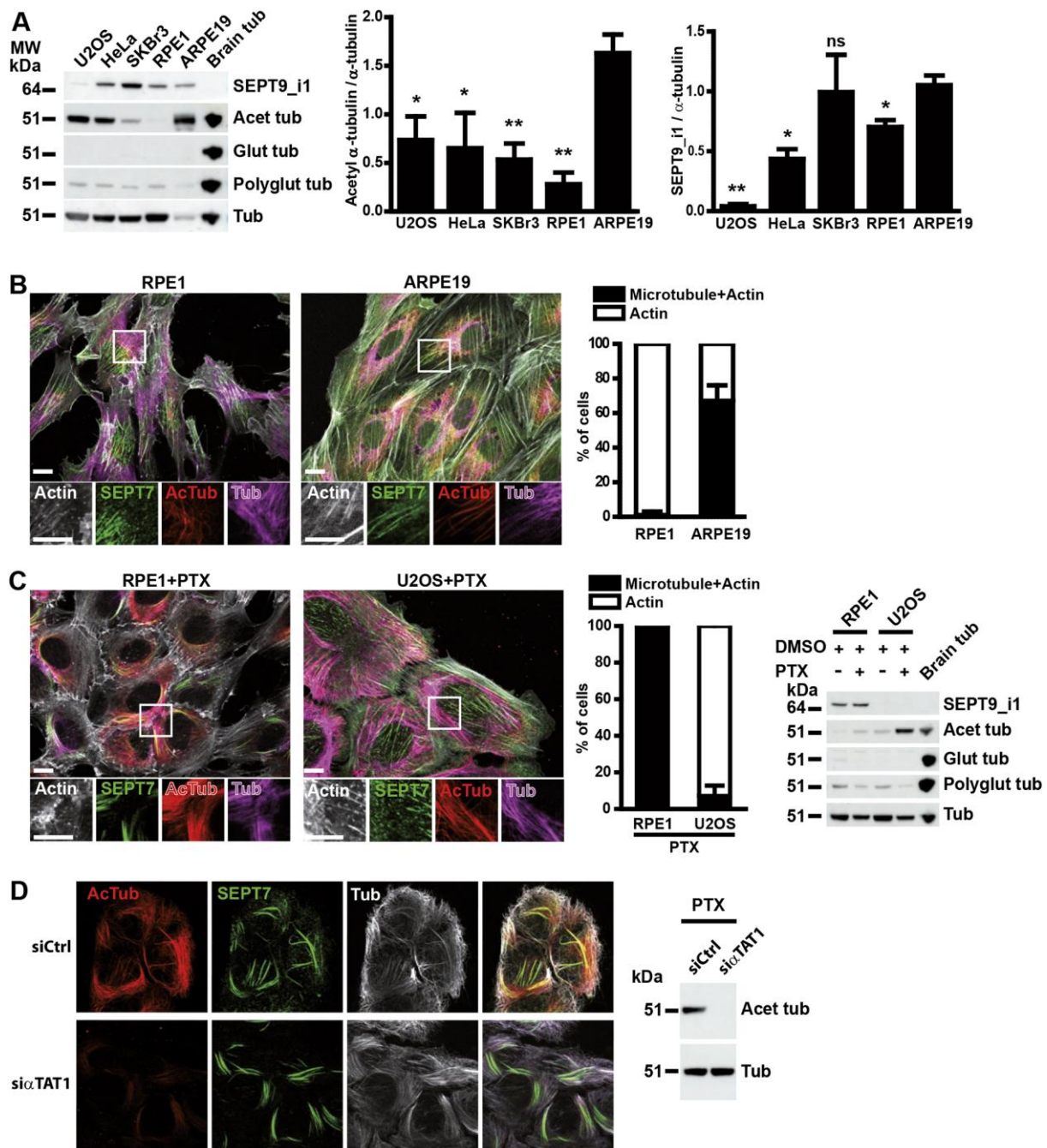


Fig. 5. Dependence of SEPT9_i1 binding to microtubules on microtubule bundling but not acetylation or polyglutamylation. (A) Left: Western blots of total protein extracts from indicated cell lines, probed for SEPT9_i1, α -tubulin acetylation on K40, glutamylation (one or two glutamate residues) and polyglutamylation of tubulin; an equivalent amount of purified porcine brain tubulin (Brain tub) was included as a positive control. Right: quantification of tubulin acetylation and SEPT9_i1 expression levels in cell lines relative to total α -tubulin Western blots. Results are from three independent determinations. Unpaired, two-tailed t-test with Welch's correction, * p < 0.05, ** p < 0.01, tubulin acetylation/SEPT9_i1 levels relative to ARPE19. (B) Left: Co-localization by immunocytochemistry of SEPT7 with microtubules and/or actin fibers in interphase RPE1 and ARPE19 cells; scale bars 10 μ m, insets: two-fold

zooms of framed regions. Right: quantification of this co-localization from three independent experiments on a total of 90 cells (30 cells per experiments). (C) Left: Co-localization by immunocytochemistry of SEPT7 with microtubules bundles induced by paclitaxel treatment (PTX) and/or with actin fibers in RPE1 and ARPE19 cells; scale bar 10 μ m, insets: two-fold zooms of framed regions. Middle: quantification of this co-localization from three independent experiments on a total of 90 cells (30 cells per experiments). Right: Western blots as described in (A) of total protein extracts of cells that were treated with vehicle alone (DMSO) or PTX. (D) Left: Co-localization by immunocytochemistry of SEPT7 with microtubules bundles induced by paclitaxel treatment (PTX) in RPE1 cells transfected with a control siRNA (siCtrl) or a siRNA against the α -tubulin acetyl transferase 1 (α TAT1); scale bar 10 μ m. Right: Western blot of total protein extracts from the same cells, showing down-regulation of α -tubulin acetylation upon α TAT1 knockdown.

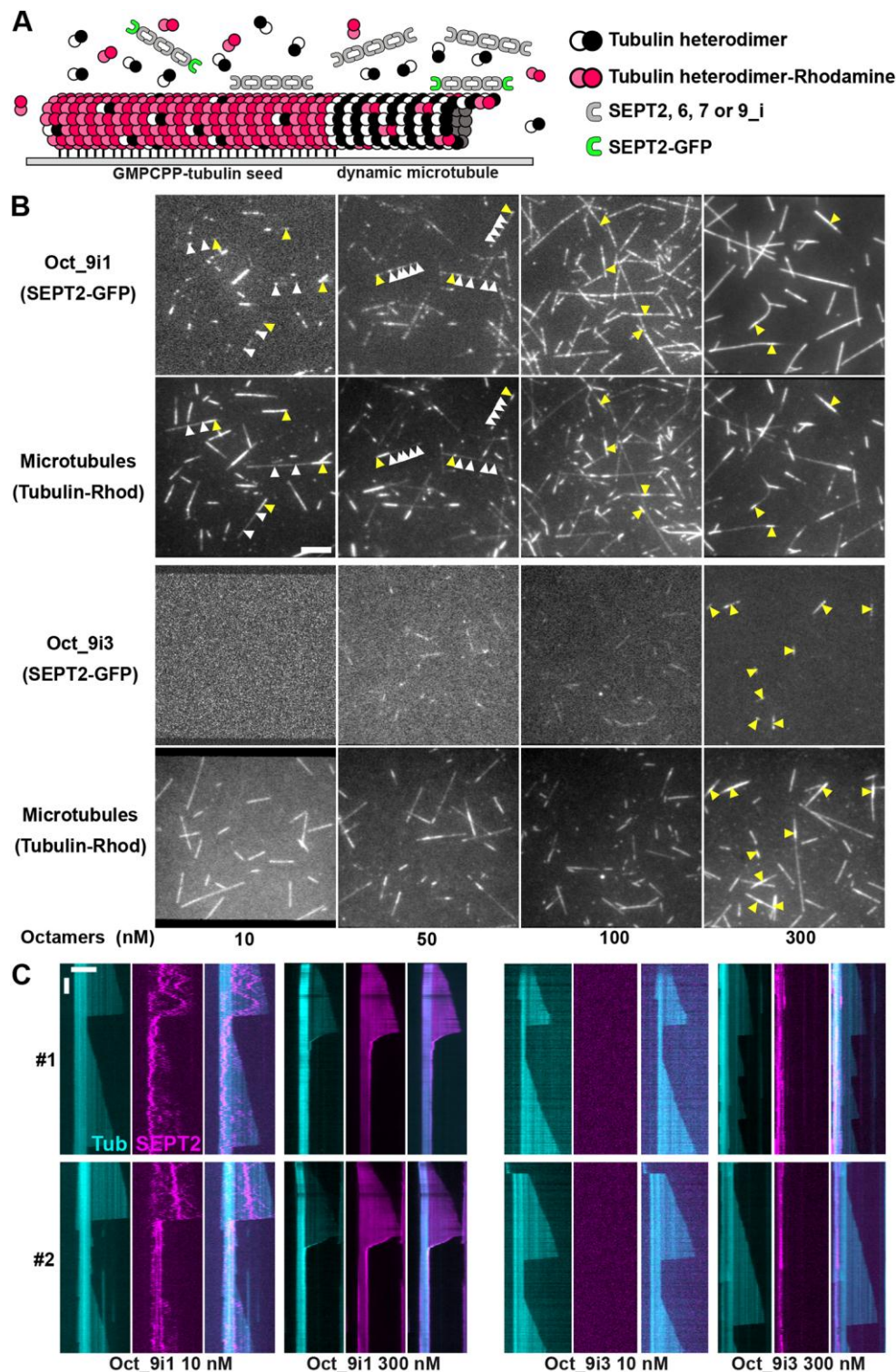


Fig. 6. Recombinant septin octamers containing SEPT9_i1 specifically bind microtubules *in vitro*. (A) Schematic representation of the *in vitro* assay. Biotinylated GMPCPP-stabilized microtubule seeds were immobilized on a streptavidin coated passivated glass coverslip, and free tubulin heterodimers (10 μ M) were added along with septin octamers (at nM concentrations, containing 10% msfGFP-labeled septins). The seeds were labelled with a higher percentage (30%) of rhodamine-tubulin heterodimers than the free tubulin

added (3-6%) to be able to distinguish the seed from the dynamic microtubules. (B) Septin octamers harboring either SEPT9_i1 or _i3 subunits (Oct_9i1 or Oct_9i3) were introduced in the chamber at the indicated concentrations and their binding observed on dynamic microtubules (examples of sporadic binding indicated by white arrow heads) and stable microtubule seeds (examples indicated by yellow arrow heads). Scale bar 5 μ m. (C) Two examples of representative kymographs of microtubules in the presence of the minimal (10 nM) or maximal (300 nM) septin octamer concentrations. False colors for rhodamine (Tub) and GFP (SEPT2) fluorescence signals were used to optimize visually the merged images. Horizontal scale bar 5 μ m; vertical scale bar 50 sec.

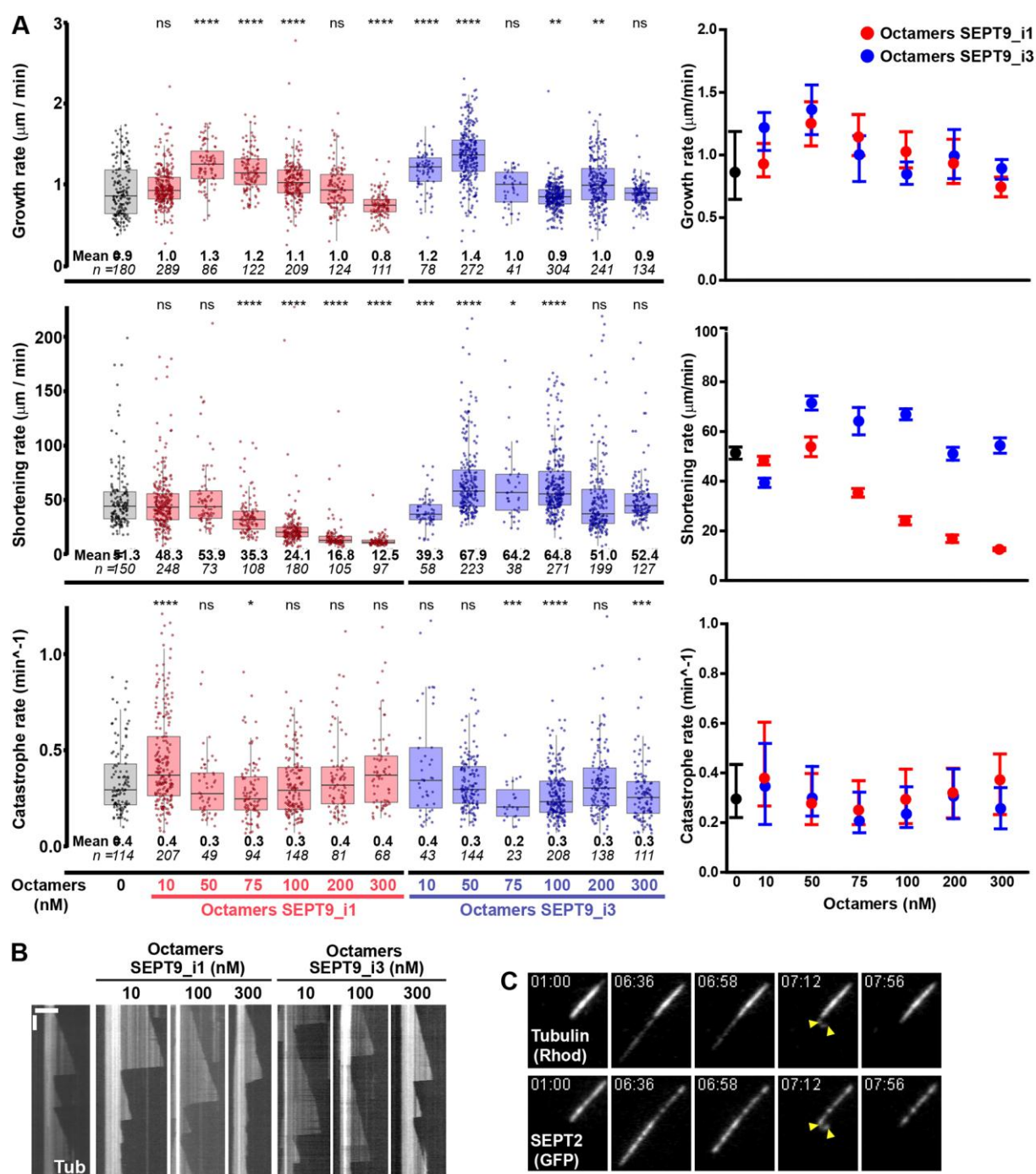


Fig. 7. Recombinant septin octamers containing SEPT9_i1 reduce the shortening rate of dynamic microtubules *in vitro*. (A) Quantitation of microtubule dynamic parameters (growth, shortening and catastrophe rates) at increasing septin octamer concentrations. (Left) Results are presented as box and whiskers plots (median value horizontal bar in each box with 5-95 percentile range) superposed with individual data points. The number of microtubules used (n) and mean value are indicated under each plot. Two-tailed t-test with Benjamini & Hochberg p-value correction with R, * $p < 0.05$, ** $p < 0.01$, *** $p < 0.001$, **** $p < 0.0001$, ns: not significant. (Right) Graphs show median values in the absence of octamers (black dots) and direct comparison in the presence of either octamers with SEPT9_i1 (red dots) or

octamers with SEPT9_i3 (blue dots) and corresponding interquartile ranges. (B) Representative kymographs (rhodamine channel for tubulin) are shown. Horizontal scale bar 5 μm ; vertical scale bar 50 sec. (C) Snapshots at indicated times (min:sec) of a depolymerizing microtubule and associated septin octamers with SEPT9_i1 (200 nM). See also Movie 3. Yellow arrow heads point at a curved structure on a depolymerizing microtubule plus-end. Scale bar 5 μm .

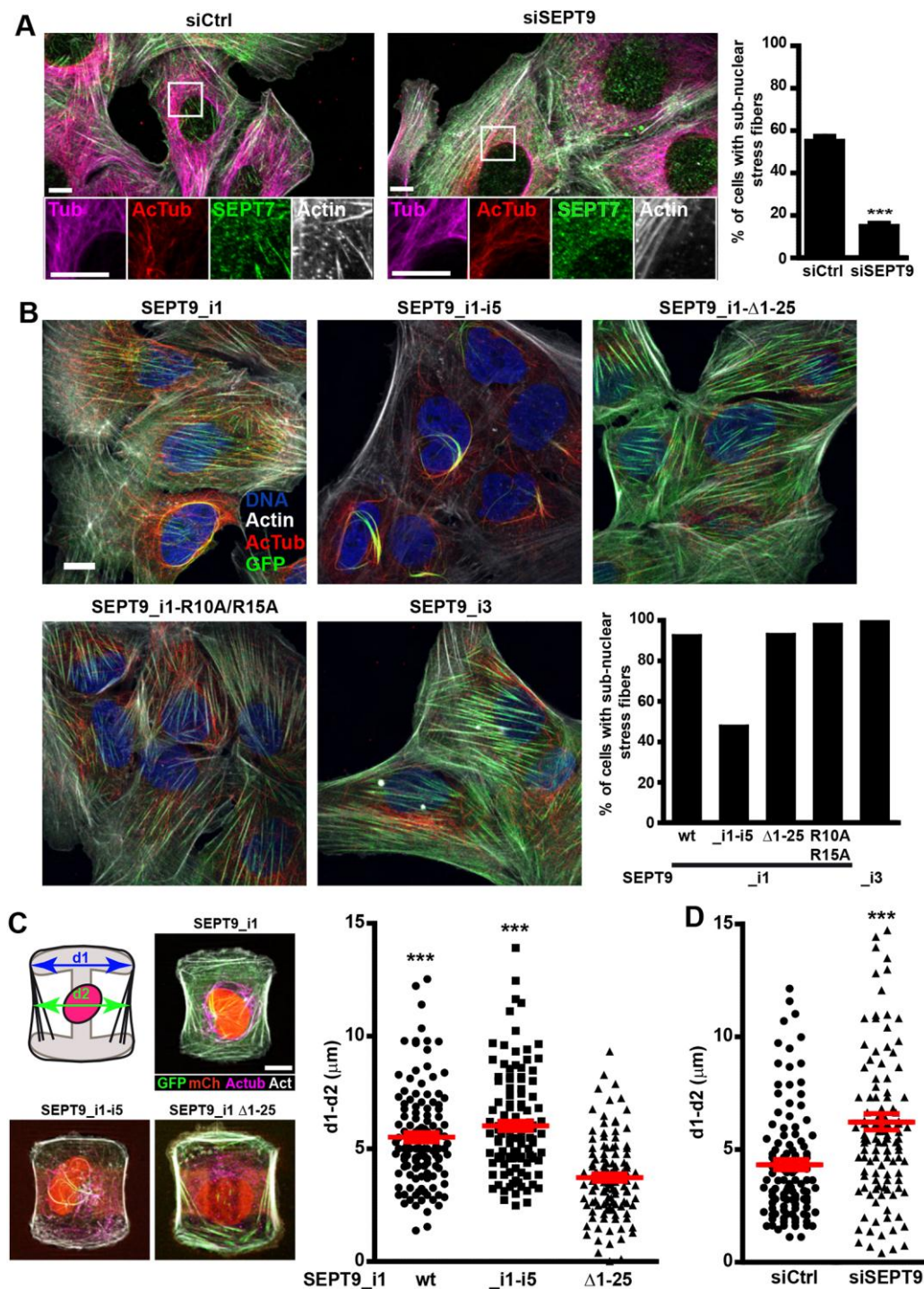


Fig. 8. Impact on actin cytoskeleton and cell shape of septin octamer sequestration by microtubules via SEPT9_i1 MBD. (A) Analysis of the presence of sub-nuclear actin fibers in U2OS transfected by either siCtrl or siSEPT9. (Left) Representative images of the colocalization of SEPT7 with sub-nuclear actin stress fibers are shown. Scale bar 10 μm, insets: two-fold zooms of frames region. (Right) Quantification from three independent experiments on a total of 90 cells per condition (30 cells per experiments). Unpaired, two-tailed t-test with Welch's correction, *** $p < 0.0005$ SEPT7(B) Analysis and representative images of the presence of sub-nuclear actin fibers in U2OS cell lines stably expressing the indicated GFP-

tagged SEPT9_i1 constructs and the histone mCherry-H2B fusion protein. Results are from a single determination on 100 cell images per cell lines. (C) Morphological analysis of U2OS cell lines stably expressing the indicated SEPT9_i1 constructs and the histone mCherry-H2B fusion protein, adhering to H-shaped micropatterns. d1: average maximum width of 35.170 μm measured on four empty H micropatterns; d2: observed width of single adherent cells at mid-maximal height of the H micropatterns. Representative images of merged fluorescence channels of the three U2OS derived cell lines are shown. Scale bar is 10 μm . Right: measurements of the difference between d1 and d2, showing a higher value when septins bind to microtubules, due to a reduction of the cell width at mid-maximal height. Results are from two independent experiments on a total of 120 cells (60 cells per experiment). Unpaired, two-tailed t-test with Welch's correction, *** $p < 0.0005$. Red lines represent mean values \pm SEM. (D) Measurements of d1-d2, as described in (C), in U2OS cells transfected by either siCtrl or siSEPT9 showing that SEPT9 knockdown reduces cell width at mid-maximal height. Results are from three independent experiments on a total of 120 cells (40 cells per experiment). Unpaired, two-tailed t-test with Welch's correction, *** $p < 0.0005$.

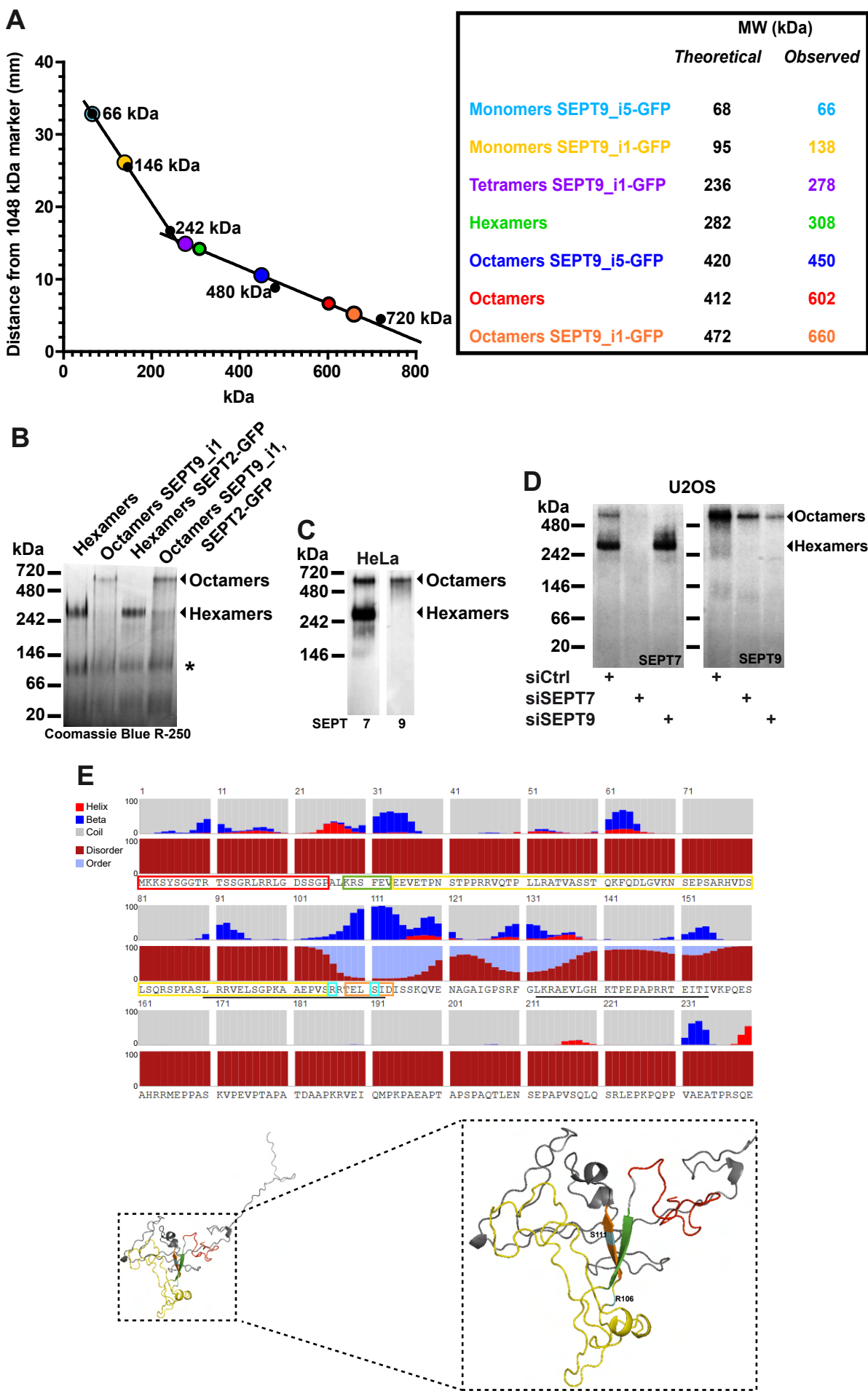


Fig. S1. Separation of septin complexes on native blue gels and detection by Western blot, and structure prediction of SEPT9_i1 region 1-251. (A) Relation between migration distance of native septin complexes from the top of the 4-16% acrylamide gradient gels and migration of MW markers; each data point represents the average of two or three independent determinations. Right: table presenting observed apparent MW and theoretical MW of the different complexes. (B) Recombinant septin hexamers and octamers were run on gradient native gels and were detected by Coomassie blue staining; the asterisk indicates the migration position of putative septin monomers. (C) Native protein extracts from Hela cells were run on native gels and blotted on a PVDF membrane; septin hexamers and octamers were detected by WB. (D) U2OS cells were knocked down for SEPT7 or SEPT9 and native extracts were analyzed as in (C). (E) Top, prediction of secondary structures and disorder in SEPT9_i1 sequence only 1-240 is shown using RaptorX Property Prediction server. Imperfect repeats are underlined with a black line. Bottom, 3D model#2 of the same sequence using RaptorX Contact Predict server. The same color code is used for framed sequences and corresponding portions of the 3D model: red, MBD domain; green, a β -sheet just downstream of MBD; yellow, sequence between the first β -sheet in green and the R106 residue; orange, second β -sheet just downstream of R106; cyan, R106 and S111 residues that are mutated to W and F in HNA patients, respectively.

A



B



Fig. S2. Protein sequence conservation of the SEPT9_i1 MBD. (A) Alignment of SEPT9_i1 sequences grouped by phylogenetic proximity: birds and reptiles are highlighted in green and mammals in shades of blue (quadrupeds in dark blue, rodents in purple, and primates in turquoise). Amino acid residues are highlighted based on Clustal X color-coding. A conservation score histogram for each position is presented below the alignments of sequences; under each column is indicated the numerical index reflecting the conservation of physico-chemical properties of amino acid residues (asterisk : 100% identical residues, plus sign: alternative residues with conserved properties). Columns exhibit a color shading coding from the maximal conservation index (11=asterisk) in pure yellow to the minimal conservation index (2) in dark brown. SEPT9_i1 1-25 sequences were recovered using the PSI-BLAST tool and the human sequence as the seed, imported in Jalview, aligned with Mafft (redundant and truncated sequences were eliminated), and grouped by phylogenetic proximity by BLOSUM52; the two highly conserved arginine residues R10 and R15 mutated in this study are indicated at the top of alignments. (B) Consensus logo of the SEPT9_i1 MBD was generated using Jalview.

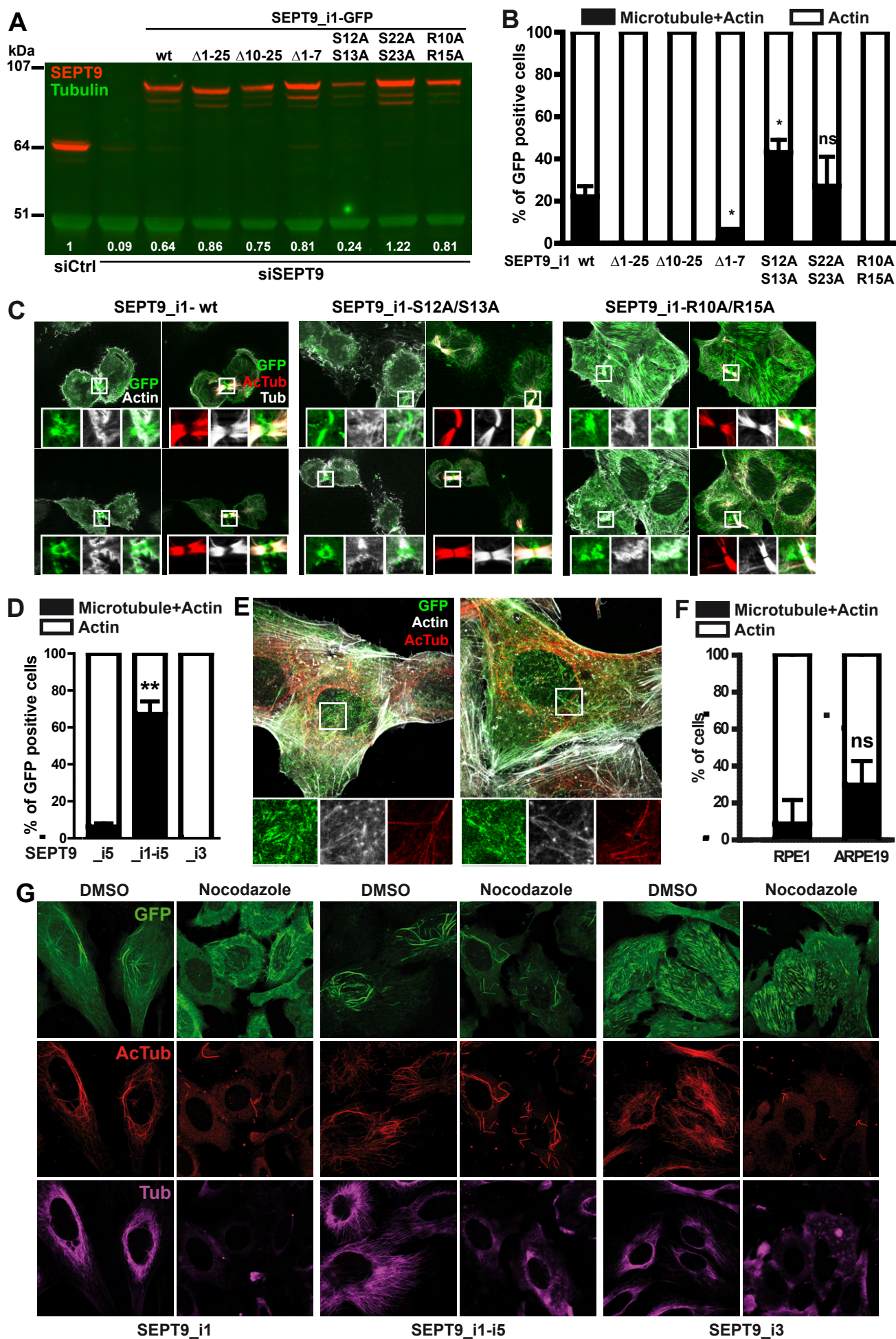


Fig. S3. Cellular localization of SEPT9 by immunocytochemistry. (A) Fluorescent detection of SEPT9 and tubulin on a Western blot of total protein extracts from U2OS cells transiently transfected by a control siRNA (siCtrl) or co-transfected with an siRNA against the 3'UTR region of SEPT9 mRNA (siSEPT9) and with the indicated constructs (described in Fig. 2B). Numbers at the bottom of each lane indicate the levels of expression of SEPT9 constructs relative to those of endogenously expressed SEPT9 (first lane), quantified on this WB. (B) Percentage of U2OS cells, expressing the indicated SEPT9-GFP constructs, displaying co-localization of SEPT9 with microtubules + actin fibers (black) or only actin fibers (white) during cytokinesis, was determined from three independent experiments based on a total of 90 cells (30 cells per experiment). Unpaired, two-tailed t-test with Welch's correction, * $p < 0.05$, ns: not significant, microtubule + actin localization relative to SEPT9_i1 wt. (C) Representative images of cells in cytokinesis. Insets are two-fold zoomed regions framed by a white square in the corresponding original images. (D) Percentage of U2OS cells transfected with the indicated SEPT9-GFP constructs displaying co-localization of SEPT9 with microtubules and actin fibers or only actin fibers during cytokinesis was determined from three independent experiments based on a total of 90 cells (30 cells per experiment). Unpaired, two-tailed t-test with Welch's correction, ** $p < 0.01$, microtubule + actin localization relative to SEPT9_i5. (E) Representative images of U2OS cells expressing SEPT9_i5-GFP. Insets are 2.5-fold zoomed regions framed by a white square in the corresponding original images. (F) The percentage of cells displaying co-localization of SEPT9 with microtubules + actin fibers or only actin fibers during cytokinesis in RPE1 and ARPE19 cell lines was determined from three independent experiments based on a total of 90 cells (30 cells per experiment). Unpaired, two-tailed t-test with Welch's correction. (G) Representative images of U2OS cells transfected with the indicated SEPT9-GFP constructs and treated by either vehicle (DMSO) or 10 μ M nocodazole for two hours.

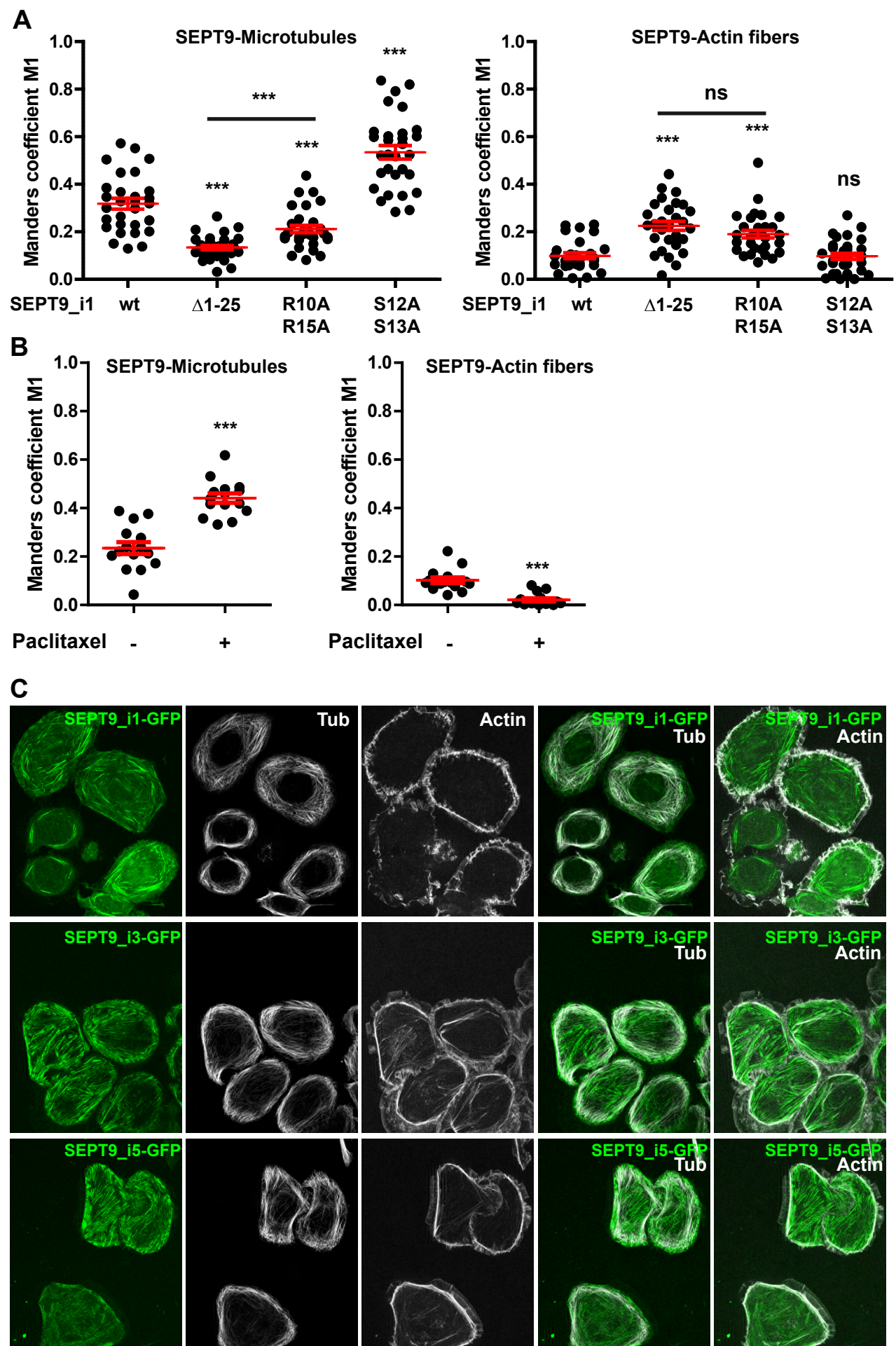


Fig. S4. Quantitation of the extent of SEPT9_i1 wt and mutant co-localization with microtubules or actin fibers within individual cells. (A) Manders M1 coefficients for co-localization of indicated SEPT9-GFP constructs expressed in SEPT9 knockdown U2OS cells with microtubules or actin fibers. Analysis was performed in 30 individual cells for each condition. (B) Manders M1 coefficient for co-localization of SEPT9_i1-GFP construct transfected in SEPT9 knockdown SKBr3 cells with microtubules or actin fibers. Seventy hours after transfection, cells were treated with either 0.002% DMSO or 2 μ M paclitaxel for two hours. Analysis was performed in 15 individual cells for each condition. Unpaired, two-tailed t-test with Welch's correction, *** $p < 0.0001$, ns: not significant. (C) Microtubule immunofluorescence, fluorescent phalloidin, and GFP fluorescence images of SEPT9 knockdown SKBr3 cells transfected with SEPT9_i1, _i3 or _i5-GFP constructs and treated with paclitaxel as in (B). Scale bar 10 μ m.

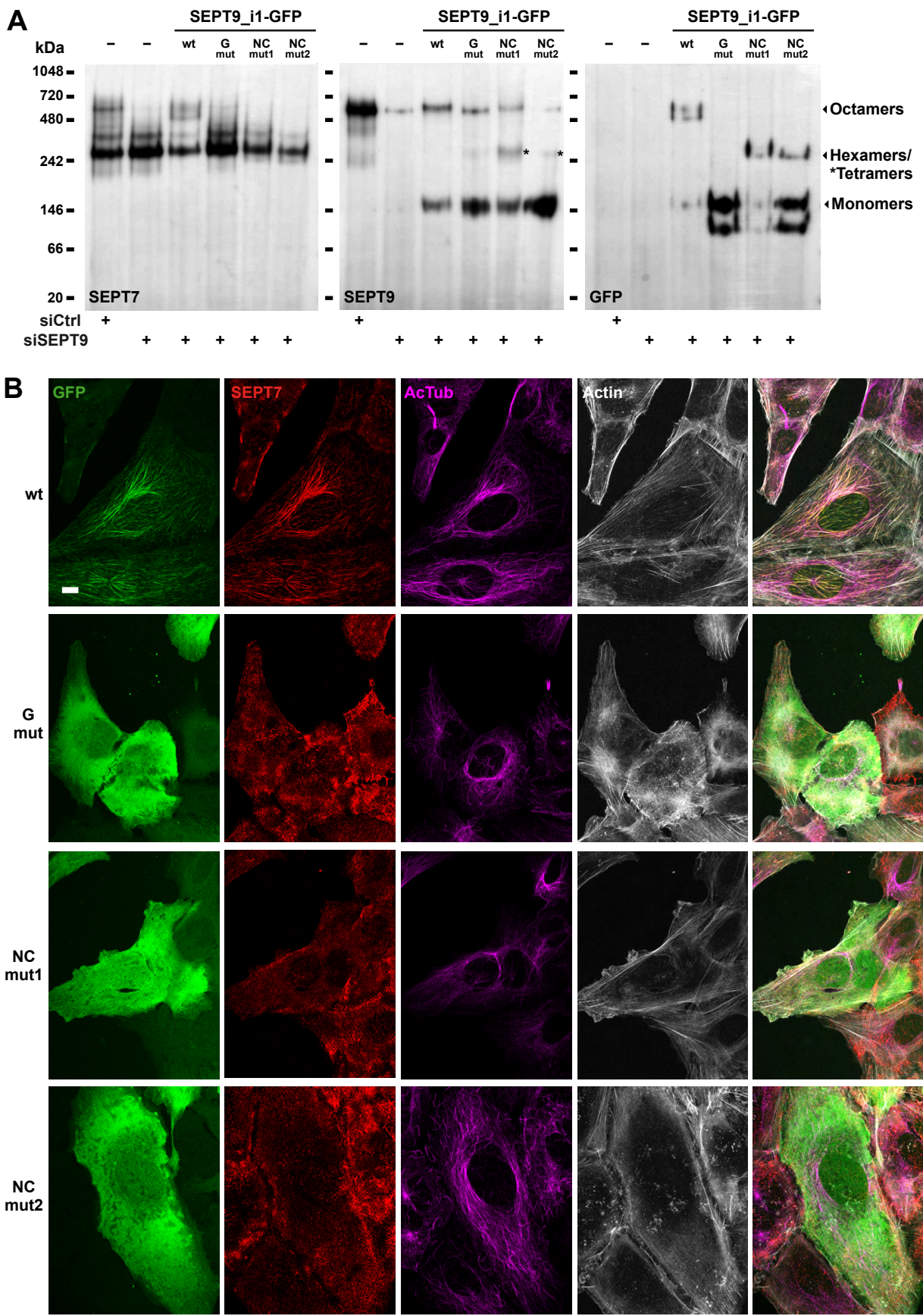


Fig. S5. Effects of SEPT9_i1 G or NC interface mutants on septin complex assembly and localization. (A) Western blots of native gels resolving septin complexes present in U2OS cells transfected with indicated siRNA and expressing SEPT9_i1 wt or SEPT9_i1 interface mutants. (B) Representative images of GFP-fluorescence based co-localization of SEPT9_i1 wt or interface mutants with SEPT7, actin and acetylated microtubules; SEPT9_i1 wt co-localized both with microtubule and actin fibers as expected, but non-octameric septin complexes containing an SEPT9_i1 interface mutant did not. SEPT7 co-localized with SEPT9_i1 wt, but localized in patches independent of the diffuse localization of SEPT9_i1 interface mutants. Scale bar 10 μ m.

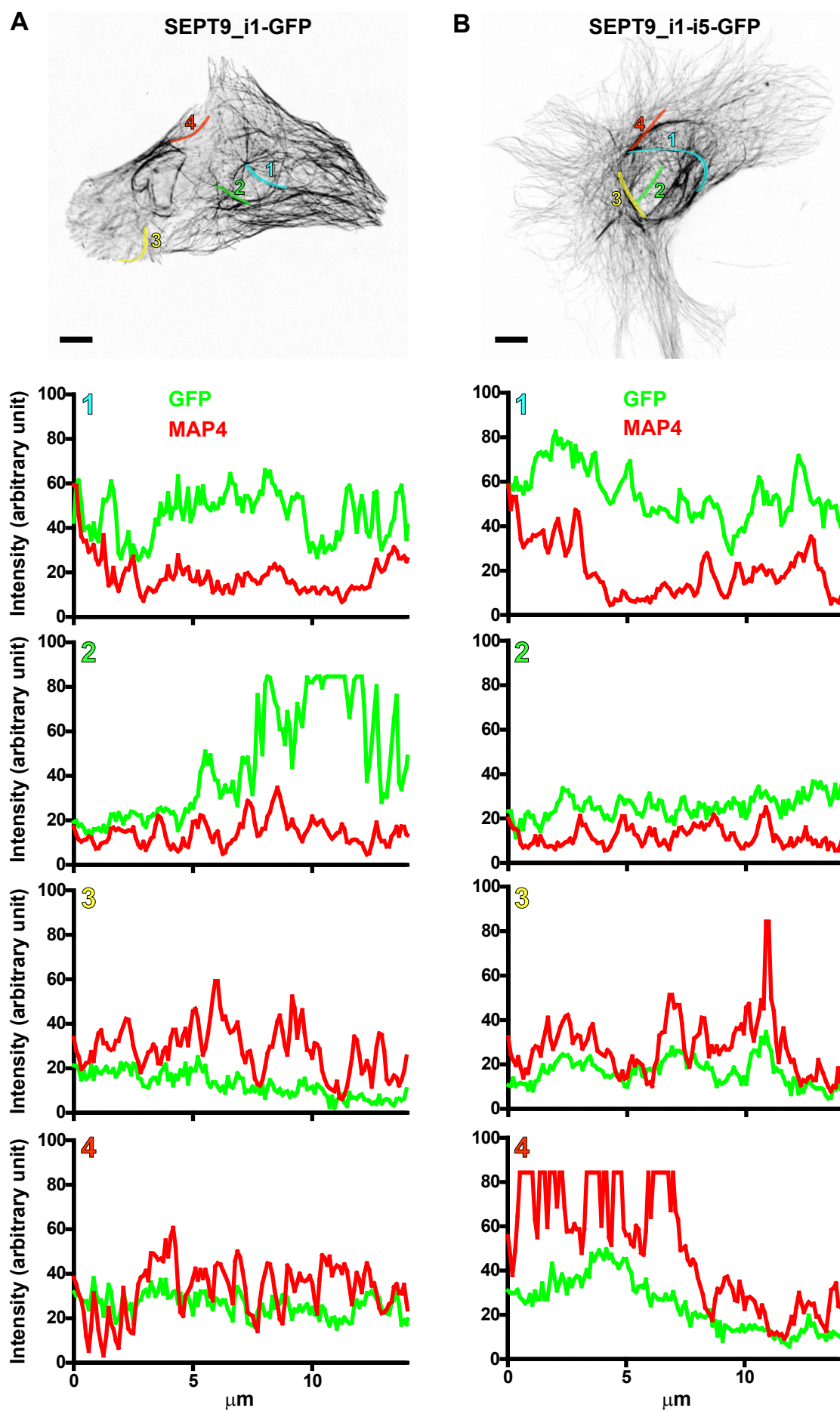


Fig. S6. MAP4 poorly localizes to microtubule bundles where SEPT9_i1 wt or SEPT9_i1-i5 accumulates. Four examples of fluorescence profiles associated with microtubule bundles (each bundle is highlighted and numbered in corresponding color in images) for MAP4 (immunofluorescence) and GFP (SEPT9 constructs) in cells expressing either SEPT9_i1 wt (A) or SEPT9_i1-i5 (B) are presented under the images of cells from Fig. 4B. Bundles with SEPT9_i1 or SEPT9_i1-i5 accumulation were more frequently seen towards the center of cells, near the nucleus (bundles numbered 1 and 2). Of note, in order to outline microtubule bundles, images correspond to grey scale negatives of merged images of microtubules and acetylated microtubules subpopulation (the latter is not presented in Fig. 4B).

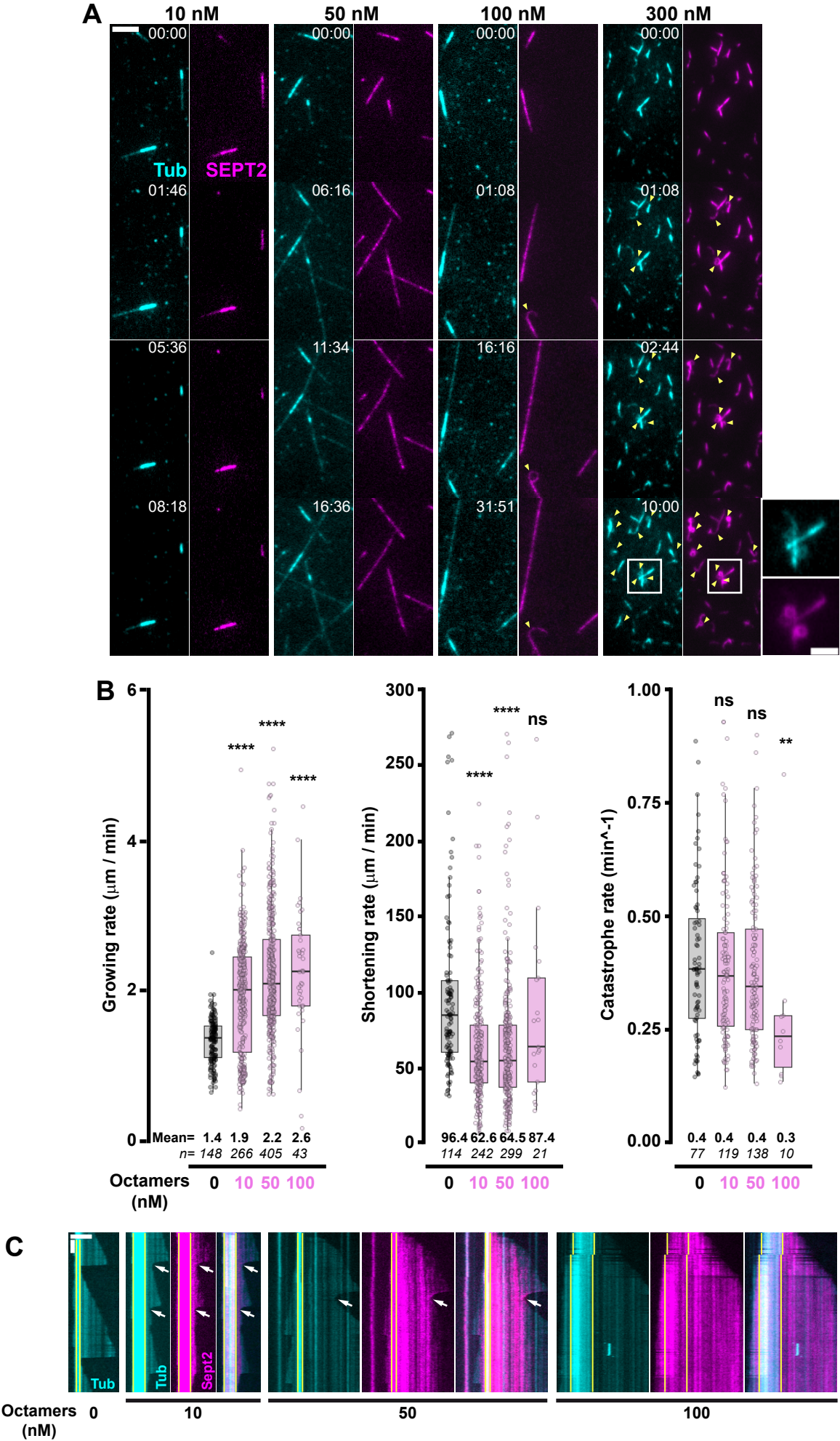


Fig. S7. Binding of octamers harboring SEPT9_i1-i5 (Oct9_i1-i5) on microtubules and their effect on microtubule dynamics. (A) Still images from time lapse TIRF movies of Oct9_i1-i5 interacting with dynamic microtubules at different concentrations in the range of 10-300 nM. Time indicated on each set of images is in min:sec. Yellow arrowheads indicate curved and loop-like structures present at the plus-ends of growing microtubules. The inset shows a close-up of these loops after 10 min with 300 nM Oct9_i1-i5. Scale bar 5 μ m in the main images and 2 μ m in zoomed framed region. (B) Quantitation of microtubule dynamic parameters (growth, shortening and catastrophe rates) at increasing septin octamer concentrations. Results from two independent experiments are presented as whisker boxes (median value horizontal bar in each box with 5-95 percentile range) superposed with individual data points. The result of a two-tailed t-test with Benjamini & Hochberg p-value correction with R comparing each sample with the control (no octamers) is shown above each whisker box (* $p < 0.05$, ** $p < 0.01$, *** $p < 0.001$, **** $p < 0.0001$, ns: not significant). (C), Representative kymographs. Horizontal scale bar 5 μ m; vertical scale bar 50 sec. White arrows indicate rescues. Vertical yellow lines indicate the borders of the GMPCPP-stabilized microtubule seed.

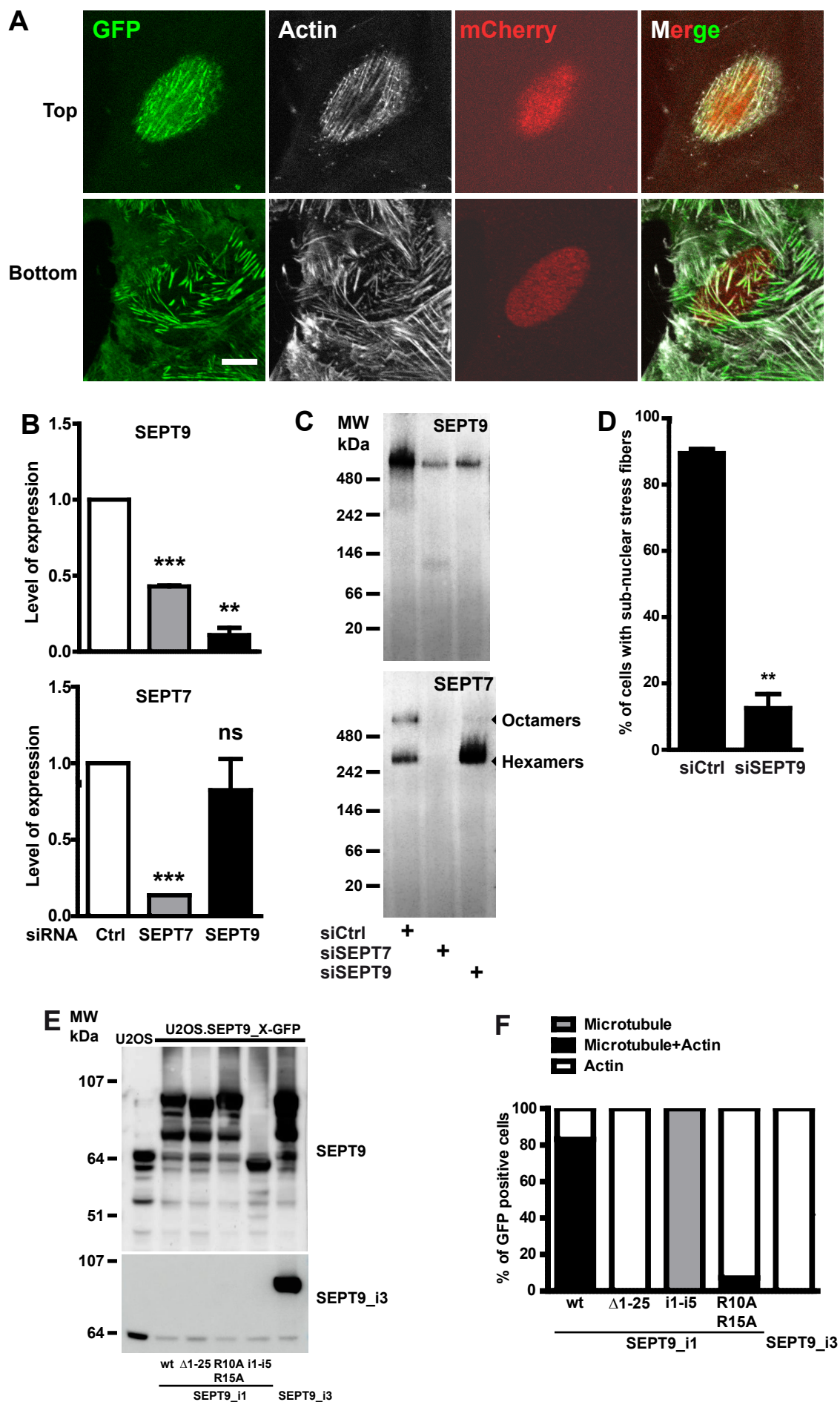


Fig. S8. Phenotyping of cells based on the presence of sub-nuclear actin fibers, and characterization of U2OS cell lines stably co-expressing SEPT9-GFP and mCherry-H2B constructs. (A) Top and bottom view of actin fibers (phalloidin-Atto 390), SEPT9_i1 (GFP), and nucleus (mCherry-H2B) in a U2OS.SEPT9_i1-GFP cell. Scale bar 10 μ m. (B) Effects of SEPT7 or SEPT9 knockdown in RPE1 cells on the relative expression of SEPT7 and SEPT9 analyzed by WB and (C) on the presence of hexamers and octamers, analyzed by Western blots of native extracts resolved on native 4-16% acrylamide native gels. In (B), Western blot signals of SEPT7 or SEPT9 expression were first normalized to the respective Western blot signals of α -tubulin and further normalized to the ratio obtained from cells transfected with Ctrl siRNA; results are from three independent experiments. Paired, two-tailed t-test with Welch's correction, ** $p < 0.01$, *** $p < 0.0005$, ns: not significant. (D) Quantification of the presence of sub-nuclear actin fibers in SEPT9 knockdown RPE1 cells KD in the absence of octamers. Results are from three independent experiments for a total of 90 cells (30 cells per experiment). Unpaired, two-tailed t-test with Welch's correction, ** $p < 0.01$. (E) Expression of SEPT9-GFP constructs (SEPT9_X-GFP) and total endogenous SEPT9 (top Western blot) and expression of SEPT9_i3-GFP constructs and endogenous SEPT9_i3 (bottom Western blot) in U2OS cell lines stably co-expressing mCherry-H2B and SEPT9-GFP constructs (U2OS.SEPT9_X-GFP) and in the non-transfected parental U2OS cell line. (F) Percentages of cells displaying co-localization of SEPT9_X-GFP with microtubules and actin fibers in U2OS.SEPT9_X-GFP cell lines. Results are from one determination in 30 cells from each cell line.

Table S1. Microtubule dynamic parameters for conditions depicted in Fig. 6, 7.

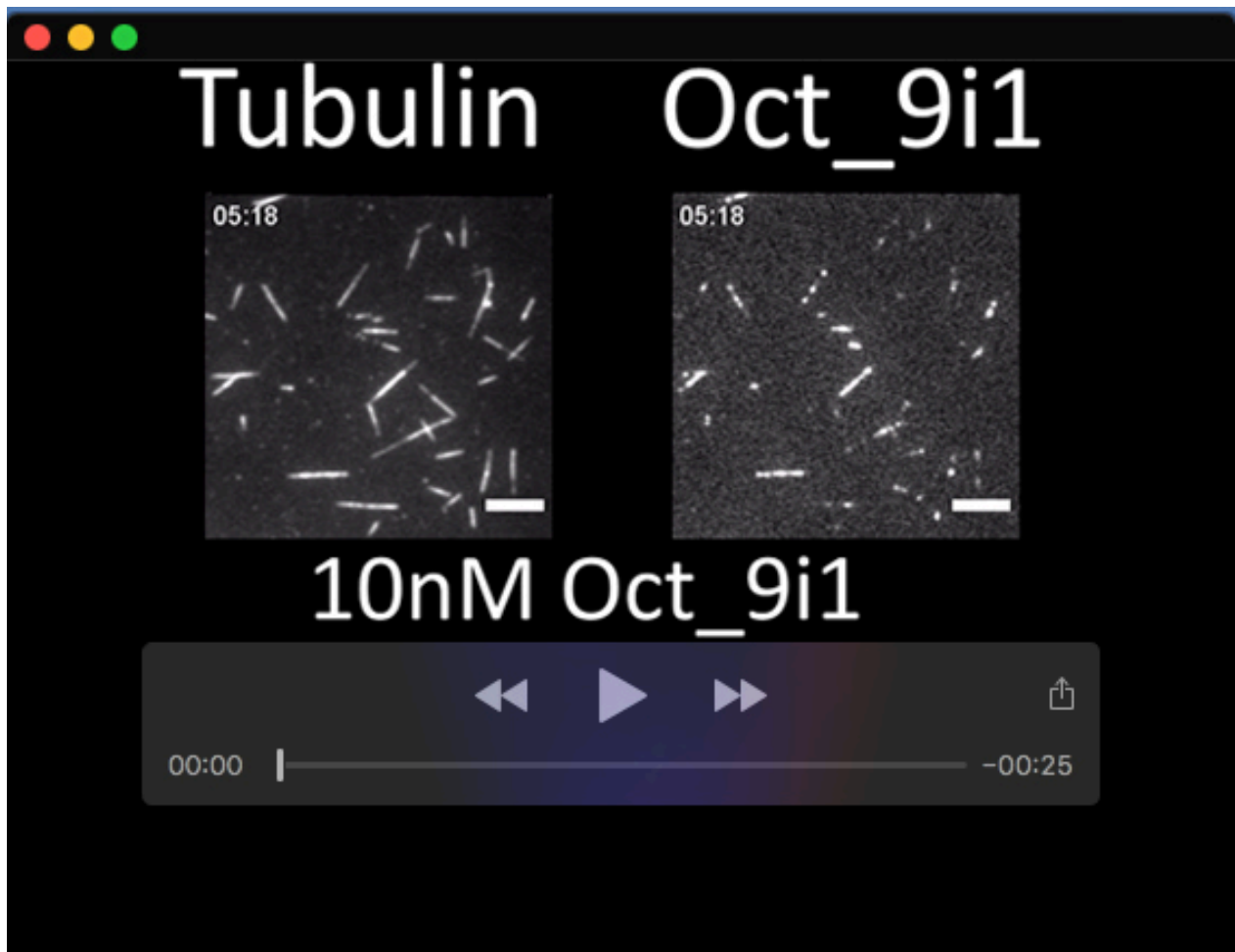
[Click here to download Table S1](#)

Table S2. Microtubule dynamic parameters for conditions depicted in Fig. S7.

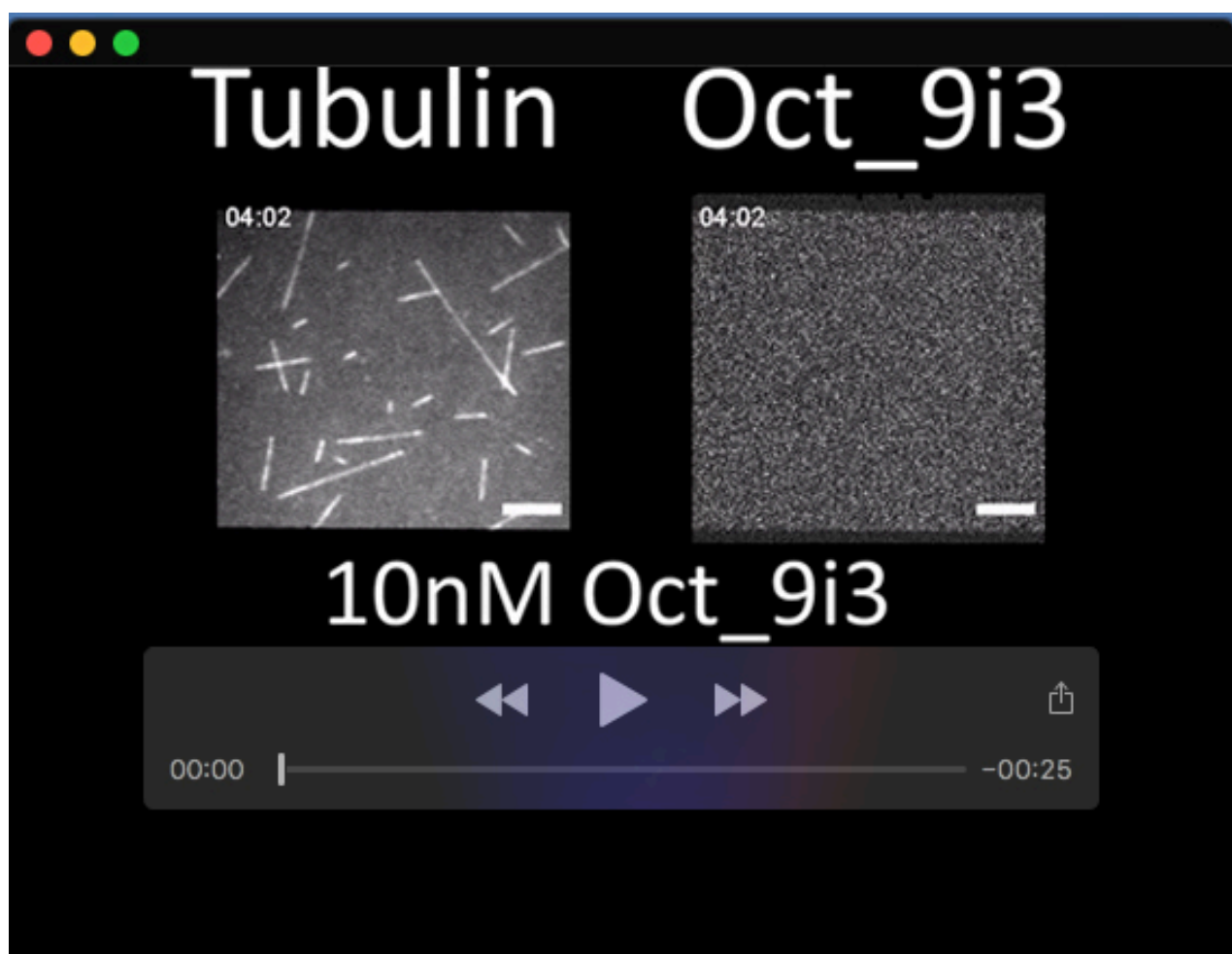
[Click here to download Table S2](#)

Table S3. Oligonucleotide primer sequences used for the generation of the plasmids used in this study. Oligonucleotides marked with an asterisk are shared among several constructs, but are listed only once.

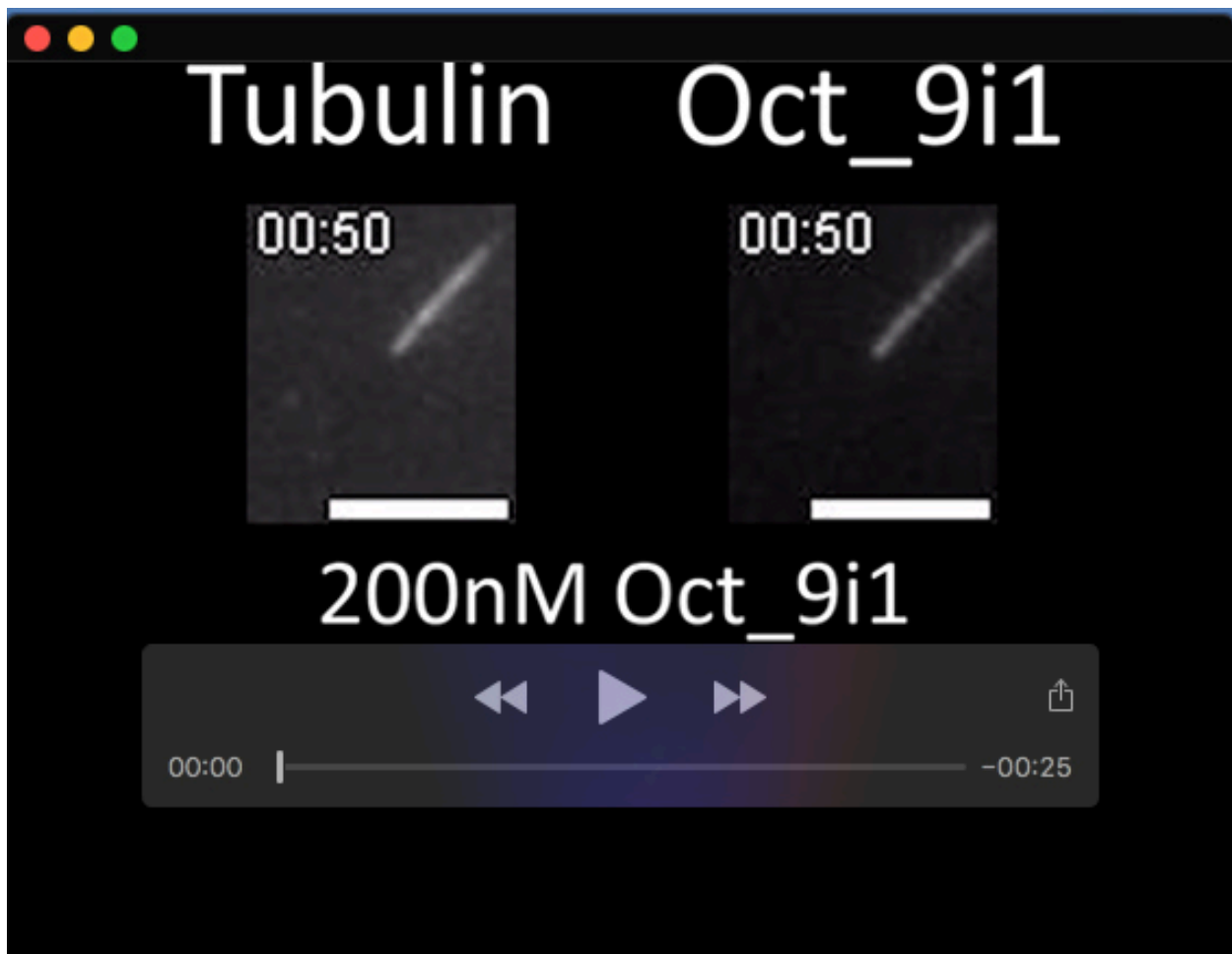
[Click here to download Table S3](#)



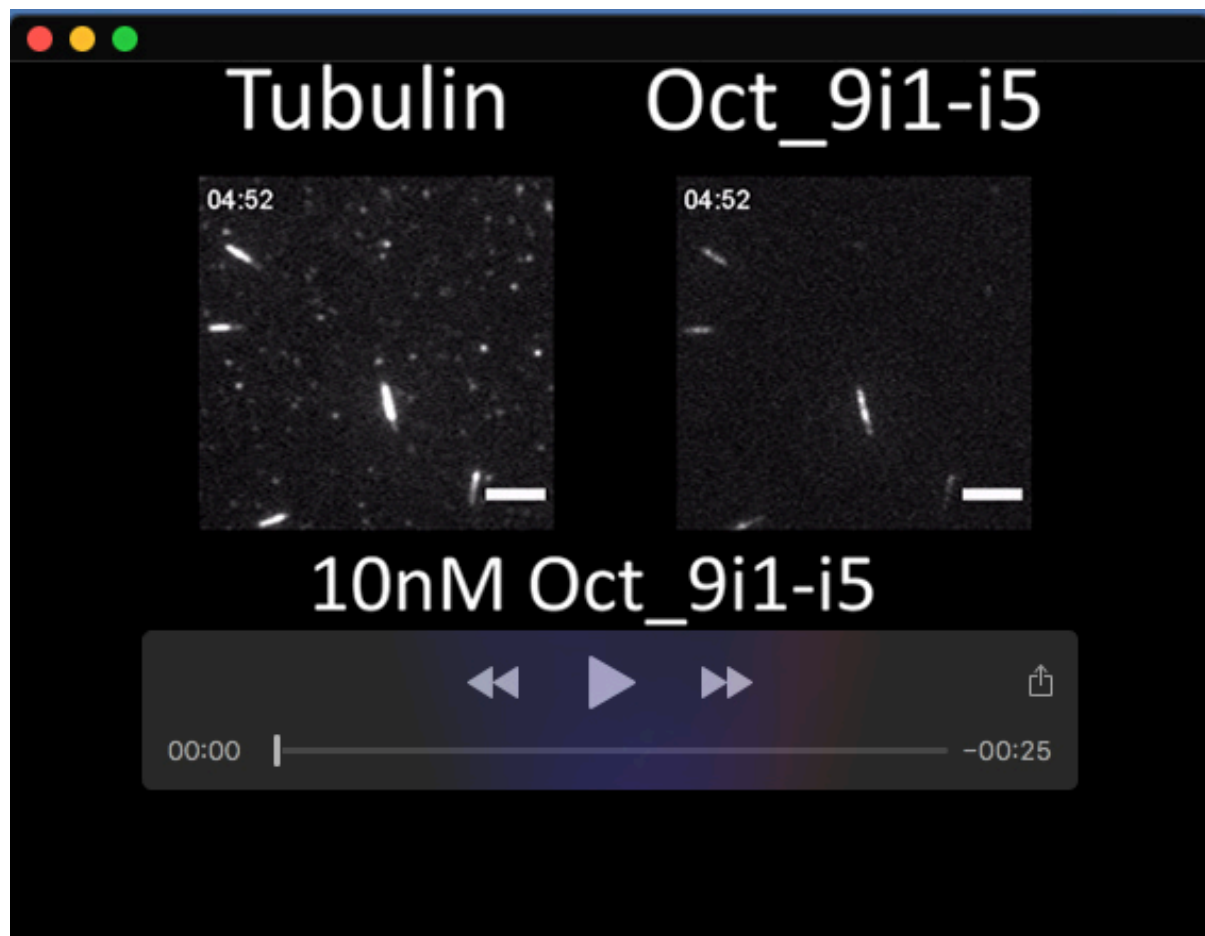
Movie 1. Dynamics of septin octamers harboring SEPT9_i1 (Oct_9i1) binding with microtubules *in vitro*. Series of videos corresponding to each of the 10 to 300 nM concentrations of Oct_9i1 that were used. Scale bar 5 μ m.



Movie 2. Dynamics of septin octamers harboring SEPT9_i3 (Oct_9i3) binding with microtubules *in vitro*. Series of videos corresponding to each of the 10 to 300 nM concentrations of Oct_9i3 that were used. Scale bar 5 μ m.



Movie 3. Depolymerizing microtubules in presence of 200 nM of septin octamers harboring SEPT9_i1 (Oct_9i1) *in vitro*. Series of videos corresponding to examples 1 and 2. Scale bar 5 μ m.



Movie 4. Dynamics of septin octamers harboring SEPT9_i1-i5 (Oct9_i1-i5) binding with microtubules *in vitro*. Series of videos corresponding to each of the 10 to 300 nM of Oct_9i1-i5 that were used. Scale bar 5 μ m.